



UNIVERSIDADE ESTADUAL DE CAMPINAS  
Instituto de Física “Gleb Wataghin”

**Jets, Vortices and  $\Lambda$  Polarization  
in the Quark-Gluon Plasma**

Jatos, Vórtices e Polarização de  $\Lambda$   
no Plasma de Quarks e Glúons

JOÃO GUILHERME PRADO BARBON

Campinas  
2021

JOÃO GUILHERME PRADO BARBON

Jets, Vortices and  $\Lambda$  Polarization  
in the Quark-Gluon Plasma

Jatos, Vórtices e Polarização de  $\Lambda$   
no Plasma de Quarks e Glúons

Dissertação apresentada ao Instituto de Física  
“Gleb Wataghin” da Universidade Estadual de  
Campinas como parte dos requisitos exigidos para  
a obtenção do título de Mestre em Física, na área  
de Física.

Dissertation presented to the Institute of Physics  
“Gleb Wataghin” of the University of Campinas  
in partial fulfillment of the requirements for the  
degree of Master in Physics, in the area of Physics.

Orientador: Jun Takahashi

Este exemplar corresponde à versão  
final da dissertação defendida por João  
Guilherme Prado Barbon, e orientado  
pelo Prof. Dr. Jun Takahashi

CAMPINAS

2021

Ficha catalográfica  
Universidade Estadual de Campinas  
Biblioteca do Instituto de Física Gleb Wataghin  
Maria Graciele Trevisan - CRB 8/7450

B234j Barbon, João Guilherme Prado, 1995-  
Jets, vortices and lambda polarization in the quark-gluon plasma / João  
Guilherme Prado Barbon. – Campinas, SP : [s.n.], 2021.

Orientador: Jun Takahashi.  
Dissertação (mestrado) – Universidade Estadual de Campinas, Instituto de  
Física Gleb Wataghin.

1. Lambda. 2. Jatos (Física nuclear). 3. Plasma de quarks e glúons. 4.  
Vórtices. I. Takahashi, Jun, 1971-. II. Universidade Estadual de Campinas.  
Instituto de Física Gleb Wataghin. III. Título.

Informações para Biblioteca Digital

**Título em outro idioma:** Jatos, vórtices e polarização de lambda no plasma de quarks e glúons

**Palavras-chave em inglês:**

Lambda

Jets (Nuclear physics)

Quark-gluon plasma

Vortex

**Área de concentração:** Física

**Titulação:** Mestre em Física

**Banca examinadora:**

Jun Takahashi [Orientador]

Arlene Cristina Aguilar

Marcelo Gameiro Munhoz

**Data de defesa:** 22-12-2021

**Programa de Pós-Graduação:** Física

**Identificação e informações acadêmicas do(a) aluno(a)**

- ORCID do autor: <https://orcid.org/0000-0003-0486-3156>

- Currículo Lattes do autor: <http://lattes.cnpq.br/5920502849461306>

MEMBROS DA COMISSÃO JULGADORA DA DISSERTAÇÃO DE Mestrado DE JOÃO GUILHERME PRADO BARBON - RA 262760 APRESENTADA E APROVADA AO INSTITUTO DE FÍSICA “GLEB WATAGHIN”, DA UNIVERSIDADE ESTADUAL DE CAMPINAS, EM 22/ 12/ 2021.

COMISSÃO JULGADORA:

- Prof. Dr. Jun Takahashi - Presidente e Orientador (IFGW / UNICAMP)
- Profa. Dra. Arlene Cristina Aguilar (IFGW / UNICAMP)
- Dr. Marcelo Gameiro Munhoz

**OBS.:** Ata da defesa com as respectivas assinaturas dos membros encontra-se no SIGA/Sistema de Fluxo de Dissertação/Tese e na Secretaria do Programa da Unidade.

CAMPINAS

2021

---

# Acknowledgements

---

At first I am specially grateful for my supervisor Prof. Dr. Jun Takahashi for all the knowledge, support and patience invested towards my formation. His guidance and important advices will surely be valuable for both my personal and professional life. I would also like to thank Prof. Dr. David Dobrigkeit Chinellato and Prof. Dr. Giorgio Torrieri, from the University of Campinas, Prof. Dr. Michael Lisa, from The Ohio State University and Prof. Dr. Chun Shen, from Wayne State University, for the suggestions and recommendations made during this project.

This project would not have been possible without my friend Dr. Willian M. Serenone, who collaborated with me in this project, helped with his physics and programming expertise, and contributed with good conversations during the coffee breaks.

I would like to extend my sincere thanks to the professors of the Instituto de Física “Gleb Wataghin” (IFGW), Profa. Dra. Arlene Cristina Aguilar, Prof. Dr. Ernesto Kemp and Prof. Dr. Sandro Guedes de Oliveira for accompanying me in the evaluation committees for my qualify examination and dissertation pre-requisite examination.

I would like to acknowledge the financial support from São Paulo Research Foundation (FAPESP) through the Grant No. 2019/16293-3. Also, the initial founding from the Ministry of Science, Technology and Innovation through the National Council for Scientific and Technological Development (CNPq) under the Grant No. 136395/2019-8. In addition, I thank IFGW and the University of Campinas for the great structure and services offered.

I thank my parents, for always supporting my choices and encouraging me throughout my academic life, my Ma. Bianca Maria Silveira de Oliveira, for being such a loving and amazing woman in my life, the friends from the HadrEx group and from the IFGW, with whom I had great discussions and a great time.

---

# Resumo

---

Nos estgios iniciais de uma coliso de ons pesados, os quarks e glons esto em um estado desconfinado conhecido como Plasma de Quarks e Glons (do ingls Quark-Gluon Plasma - QGP). Neste estado, acredita-se que a matria se comporta como um fluido fortemente acoplado. Um jato de partculas formado nas proximidades pode interagir diretamente com esse meio, depositando energia e formando estruturas de vorticidade dentro do fluido. Neste trabalho, apresentamos o estudo dos efeitos causados pela termalizao da energia e do momento de um jato dentro do QGP. O momento depositado cria um gradiente de velocidade no fluido, formando anis de vorticidade e criando uma polarizao de partculas Lambda na fase de hadronizao. Em nosso modelo, usamos uma regio de alta densidade de energia como uma aproximao para o jato, representado a termalizao deixada por ele no plasma. Este processo  simulado usando um cdigo de hidrodinmica viscosa  $(3 + 1)D$  de segunda ordem. Tambm fazemos um estudo sistemtico da evoluo da termalizao do jato dentro do plasma, analisando propriedades tais como a densidade de energia local e a vorticidade em funo de diferentes valores de viscosidade do fluido. O anel de vorticidade criado pela perturbao do jato no Plasma de Quarks e Glons est diretamente relacionado com a polarizao das partculas Lambda. Usamos este observvel de polarizao para criar um observvel  $\overline{\mathcal{R}}_\Lambda^{\hat{t}}$  que seleciona apenas as contribuio de vorticidade geradas pelo jato. Estudamos tambm o comportamento de  $\overline{\mathcal{R}}_\Lambda^{\hat{t}}$  para diferentes cenrios de simulao hidrodinmica.

---

# Abstract

---

In the initial stages of a heavy-ion collision, the quarks and gluons are in a deconfined state, referred to as Quark-Gluon Plasma (QGP). This state is believed to behave as a strongly coupled fluid. A jet formed nearby can interact directly with this medium, depositing energy and forming a vortical structure inside the fluid. In this work, we present the study of the effects caused by the thermalization of the jet energy and momentum in the plasma. The momentum deposited in the medium will create a large velocity gradient in the fluid that will form vorticity rings, and that ultimately can cause a polarization of Lambda particles at hadronization. In our model we approximate the jet as a region of higher energy density, representing the thermalization left by it in the QGP. This system is simulated using a  $(3+1)$ D second order viscous hydrodynamic code. We also do a systematic study of the evolution of the jet thermalization inside the fluid, analyzing properties such as local energy density and vorticity response to variations in the fluid's viscosity. The vorticity ring created by the perturbation in the QGP is directly related to the polarization of the  $\Lambda$  particles. We use this polarization to build a ring observable  $\overline{\mathcal{R}}_{\Lambda}^{\ell}$  that selects only the vorticity contribution created by the jet. We also study the  $\overline{\mathcal{R}}_{\Lambda}^{\ell}$  observable for different scenarios of hydrodynamic simulations.

---

---

# Contents

---

<b>1</b>	<b>Introduction</b>	<b>10</b>
1.1	Jet as Probes to the QGP . . . . .	11
1.2	Main goal of this work . . . . .	13
<b>2</b>	<b>Overview of Heavy Ion Collisions</b>	<b>17</b>
2.1	Conventions and the Kinematic Variables . . . . .	19
2.1.1	Conventions . . . . .	20
2.1.2	Rapidity and Pseudorapidity . . . . .	21
2.2	Stages of a Collision . . . . .	23
<b>3</b>	<b>Relativistic Hydrodynamics and Vorticity in the Quark-Gluon Plasma</b>	<b>27</b>
3.1	Non-relativistic Hydrodynamics . . . . .	27
3.2	Relativistic ideal hydrodynamics . . . . .	29
3.3	Relativistic Viscous Hydrodynamics . . . . .	31
3.4	Vorticity and Polarization in the QGP . . . . .	32
3.4.1	Global Polarization and the Importance of the Lambda Particle . . . . .	33
3.4.2	Local Polarization and Vorticity . . . . .	36
3.5	The $\mathcal{R}$ Observable . . . . .	39
<b>4</b>	<b>Methodology</b>	<b>42</b>
<b>5</b>	<b>Results</b>	<b>50</b>
5.1	Systematic Study of the Jet Thermalization . . . . .	50
5.2	Final Observables . . . . .	59
<b>6</b>	<b>Final Considerations</b>	<b>64</b>
	<b>References</b>	<b>66</b>

**Appendices**

**73**

**A  $\Lambda$  polarization from thermalized jet energy**

**73**

# Introduction

In the past decades, the increasing number of high-energy experiments have broken new ground into exploring many unanswered questions in physics, ranging from the detailed description of the standard model of particles and how quarks and gluons interact, to the study of the hot and dense matter found in the early universe and in the center of neutron stars. Despite the apparent gap between these micro and macro scenarios, they are both bounded by the study of one subject, the matter in extreme conditions. In order to study such state of matter in the laboratory, a particle accelerator is used to speed up two nuclei, such as Pb–Pb or Au–Au, and collide against each other. Due to velocities close to the speed of light, each nuclei takes the form of a disk, with approximately  $14 \text{ fm}/\gamma$  of thickness, where the 14 fm stands for the approximate diameter of the Pb nuclei and  $\gamma$  for the relativistic Lorentz factor. Upon impact, the many partons - and consequently the colored quarks and antiquarks inside them - interact vigorously and create a high temperature and energy density area where quarks and gluons behave collectively. As this system evolves, the strongly coupled medium expands and flows according to the relativistic hydrodynamics, forming the Quark-Gluon Plasma (QGP), a relativistic fluid that was found to have a low viscosity to entropy ratio  $\eta/s \approx 1/4\pi$  [1, 2] and the peculiar characteristic of very high vorticity fields ( $\omega \approx 9 \times 10^{21} s^{-1}$ ). This value surpasses that of all other known fluids, such as the solar subsurface flow ( $\omega \approx 10^{-7} s^{-1}$ ) and tornado cores ( $\omega \approx 10^{-1} s^{-1}$ ) [3]. In this sense, the study of matter in extreme conditions is a state-of-art subject in both areas of high-energy and particle physics, and this work lies between these two areas. We focus on the phenomenology study of vorticity fields formed by the passing of a high momentum parton (referred to as jet) through the QGP, and its consequences on the polarization of final hadrons, more specifically the  $\Lambda$

particle. But, before we go into more detail, a brief introduction to the main concepts of this work is of good use.

## 1.1 Jet as Probes to the QGP

The discovery of the Quark-Gluon Plasma as an intermediate phase of a heavy-ion collision, with quarks and gluon forming a system of interacting particles, has brought new insights into the understanding of the behaviour of nuclear matter under extreme conditions. At first, because of the asymptotic freedom property of the QCD, it was thought that the plasma formed in a high-energy collision would be characterized by a medium with weakly interacting partons, behaving like a gas and expanding isotropically. As the studies in this area progressed, data from the Relativistic Heavy Ion Collider (RHIC) [4–6] showed that the particles emerging from the collision had a considerable amount of azimuthal anisotropy, characterized by the Fourier coefficient  $v_2$ , agreeing with a hydrodynamic description. This hydrodynamic behavior implied a strong interaction between the plasma constituents. This fact was also backed up by experiments like the one in Ref. [7], where it was shown that this elliptic flow property is only present in ensembles where particles interact via strong forces. More details about the QGP and how it's created in heavy ion collision is further discussed in Chapter 2.

The interest lied not only on the description of the QGP itself, but also in how other structures, like jet of particles, could interact with the medium, and possibly probe it. Much progress has been put forward in this sense [8–15], where the main focus revolved around the concept of jet quenching: jets with high momentum traversing the plasma will be suppressed (or quenched) and will lose energy to the medium. The analysis of the outgoing jet brought important insights regarding both thermodynamic and transport properties of the QGP [16–19]. In Fig. 1.1a we show a schematics of a jet being quenched in the QGP, while the other back-to-back component proceeds freely through the QCD vacuum. This effect was analysed by the STAR collaboration [20] in Au–Au and  $pp$  collision at  $\sqrt{s_{NN}} = 200$  GeV; in Fig. 1.1b we see the suppression of the away-side peak, indicating that the partonic interactions of Au–Au collisions form a dense medium that quenches the jet.

In a high energy collision, a jet can be identified as a collimated spray of

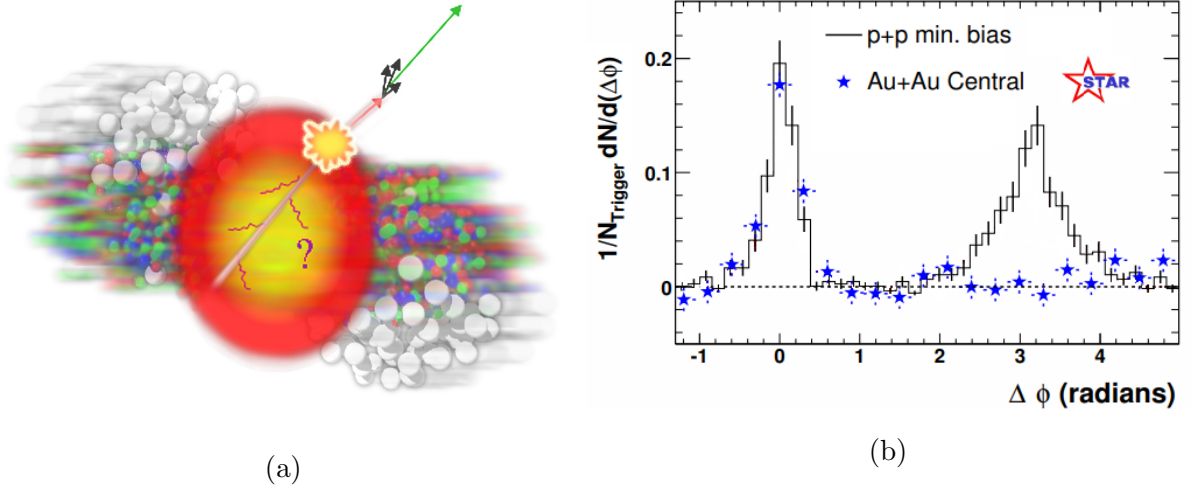


Figure 1.1: (a) Schematic representation of a jet quenching inside the Quark-Gluon Plasma. Due to hard interactions, a back-to-back jet is formed near the QGP. One component goes through the relativistic fluid, being suppressed, while the other proceeds unquenched [21]. (b) Comparison of azimuthal distribution for  $pp$  and Au–Au collision. The left peak, representing the near-side jet, is similar in both systems. The right peak, representing the away-side jet, is suppressed in the system formed in Au–Au collisions, whereas no suppression is observed in  $pp$  collisions where no QGP formation was expected. Adapted from [20].

particles. It is formed in processes such as  $qq \rightarrow qq$  or  $gg \rightarrow qq$ , where energetic quarks and gluons are formed and fragments into a shower of other quarks and gluons, subsequently hadronizing. Figure 1.2 illustrates a qualitative description of this process: steps (i) and (ii) show a pair of quark and antiquark with initial momenta in opposite directions and the formation of a color tube between them due to the strong force. This tube restricts the color field interaction between the quarks. As the distance between  $q\bar{q}$  increases, the energy stored within the tube increases, leading to the creation of a new  $q\bar{q}$  pairs (iii). This process continues to occur until there's no more energy to create a new pair of quark and antiquark (iv) and the energy is low enough for the quarks to combine to form hadrons (v). The hadronization process, therefore, consists mostly of two jets of hadrons travelling back-to-back, following the momentum direction of the initial quarks. Three and four-jet structures are less probable to happen, being formed in processes such as  $qq(gg) \rightarrow q\bar{q}g$  and  $qq(gg) \rightarrow q\bar{q}gg$ , where a gluon is originated from a quark or antiquark.

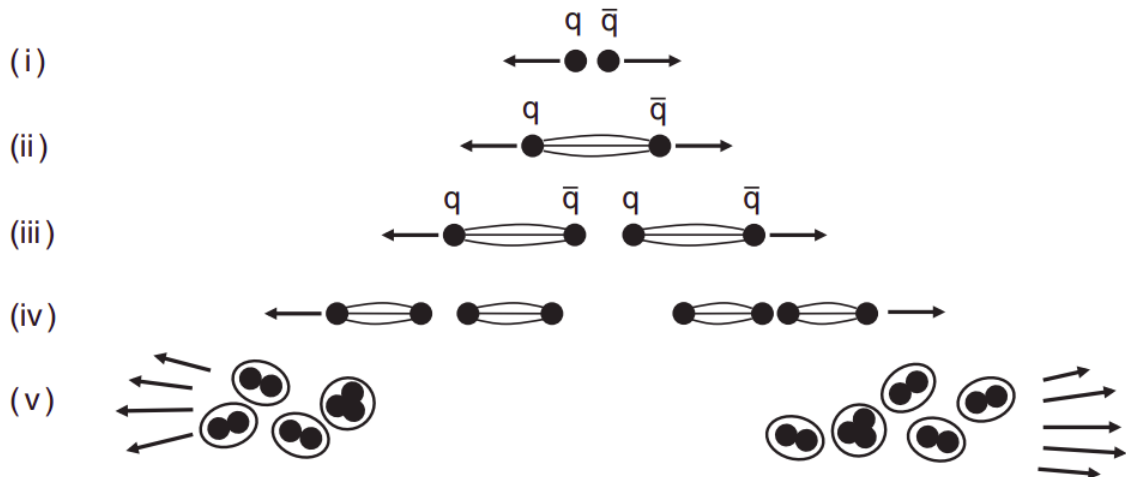


Figure 1.2: Qualitative description of the hadronization process and formation of jet of particles [22]. Steps (i) and (ii) depicts the  $q$  and  $\bar{q}$  travelling back-to-back and forming the color tube. In steps (iii) and (iv) we show the formation of new quark and antiquark pair from the existing color field, and the subsequent cascade effect forming more  $q\bar{q}$  pairs. Finally, in step (v) we have quarks combining into hadrons.

## 1.2 Main goal of this work

Throughout this work, we are mainly interested in the event of a jet quenching inside the plasma, and its consequences to the properties of the  $\Lambda$  particles emitted at hadronization phase. For instance, when a jet enters the QGP, it deposits a considerable amount of energy and momentum in the fluid, developing an overall gradient of velocity and a net momentum in its direction. From our everyday experience, we know that when a fluid, such as water or smoke, is put under a velocity gradient, it swirls and twists forming structures like eddies and smoke rings. In Fig. 1.3 we show an example of this situation, where the smoke passes with high velocity through an opening, forming a ring like shape.



Figure 1.3: Experiment showing the formation of a smoke ring. The smoke is initially undisturbed inside the plastic container. When it's pushed with high velocity against the round opening, the smoke takes the form of a ring [23].

The same principle can be expected from the jet being quenched in the QGP. We show in Fig. 1.4 an idealization of what happens in this case. We picture a scenario where a dijet is created inside the Quark-Gluon Plasma, with one component being unquenched and traveling throughout the QCD vacuum, while the other interacts with the medium, creating a vortical structure induced by the velocity gradients deposited during its evolution. In the  $xy$  plane at  $\eta = 0$ , where the jet was placed, the velocity gradients in  $x$  and in  $y$  will result in a vorticity in the positive  $\eta$  direction in the QGP above the jet, while in the negative  $\eta$  direction below the jet. As the QGP cools down, the strong coupled plasma is converted into particles in a process called hadronization. These particles created will, consequently, inherit properties from the fluid's previous state.

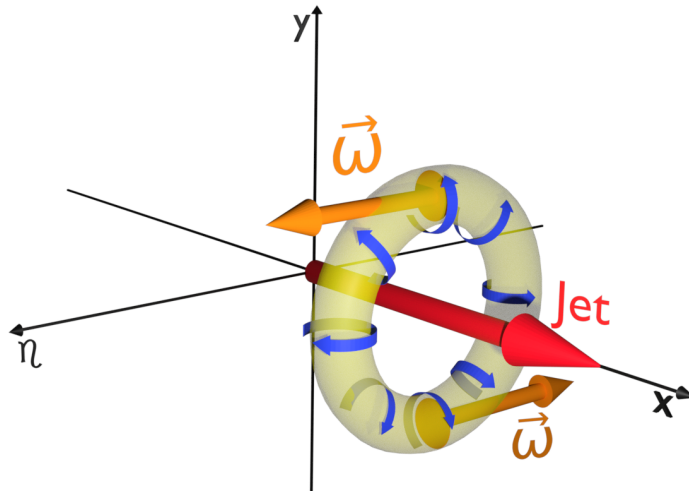


Figure 1.4: Illustration of the physical situation in which a jet travels inside the QGP. The jet component is quenched by the medium, forming a vortical structure that moves along with it. The vorticity ring indicates that the vorticity vector has a component perpendicular to the direction of the jet.

In this context, we are interested in exploring the consequences of a jet inside the QGP through an observable that can relate the rotational motion of the fluid and the property of a particle in the detector, after the collision. We achieve that by analysing the polarization of  $\Lambda$  particles [3, 24, 25], an observable that couples the vorticity created on QGP and the spin of the Lambda particle created in the freezeout phase of the QGP. With this in mind, we propose a model that uses the Lambda polarization as a mean of studying the jet quenching inside the Quark-Gluon Plasma [26]. We use a ring observable  $\overline{\mathcal{R}}_{\Lambda}^t$ , motivated by the Ref. [27], to extract information of polarization from all direction of the vorticity ring structure. We run a (3+1)D hydrodynamic simulation [28], where the jet quenching is modeled as a spherical region with high energy density placed at the center of the simulation grid, with a smooth initial condition simulating the background evolution of the QGP. We also study the systematic behavior of the medium's evolution, observing how this system responds to variations in the viscosity of the fluid.

In Chapter 3 we discuss the theoretical framework used to characterize the physical properties of the QGP, the relativistic hydrodynamics. Also, we discuss the main principles behind the vorticity and the  $\Lambda$  polarization. The methodology of the

---

jet model is described in Chapter 4, where we go over the considerations made and the simulations steps. Finally, in Chapter 5 we present our analysis of the simulations. We begin by showing a systematic study of the jet evolution, analysing the energy density and vorticity behavior as the jet moves inside the QGP, and we end with a study of the  $\Lambda$  polarization and the ring observable  $\overline{\mathcal{R}}_{\Lambda}^i$ .

# Overview of Heavy Ion Collisions

In a heavy-ion collision, two colliding nuclei, such as Pb–Pb or Au–Au, can be described as Lorentz contracted discs accelerating at each other. As they overlap, their constituent partons interact and their initial momentum is redistributed in the collision area, creating a high energy density and high entropy region. This entropy created is large, since we are going from a system with two nuclei to a system where thousands of particles are created. Thus, the quarks and gluons formed after the collision are far from equilibrium. They form a highly energetic strongly coupled system that cannot be described in terms of hadrons, but rather as a medium that has collective behavior that can be well described by relativistic hydrodynamics, resembling a fluid with low viscosity to entropy ratio of  $\sim 1/4\pi$  [1, 2]. This matter is called Quark-Gluon Plasma, and it goes through the phases of expansion and cooling as it flows hydrodynamically. In this scenario, as the fluid cools down, the energy density diminishes and reaches a threshold value to form hadrons. This entire process of heavy-ion collision is depicted in Fig. 2.1, where the stages of initial state, hard collision, plasma formation, expansion and hadronization are shown.

As we've discussed, the HIC create droplets of a relativistic fluid that, as the system evolves, forms the particles we know. This relativistic matter is believed to have been formed in the early universe, a few microseconds before the Big-bang [30, 31]. In Fig. 2.2 we show a cartoon of the current understanding of cosmological models with the different stages that our universe has undergone since the Big-bang. In this model, it is believed that the QGP was the first matter formed after about  $10^{-6}$ s, with temperature around  $10^{12}$  K. This connection between the plasma formed right after the Big-bang and the plasma formed in a heavy-ion collision provides the possibility of learning more about

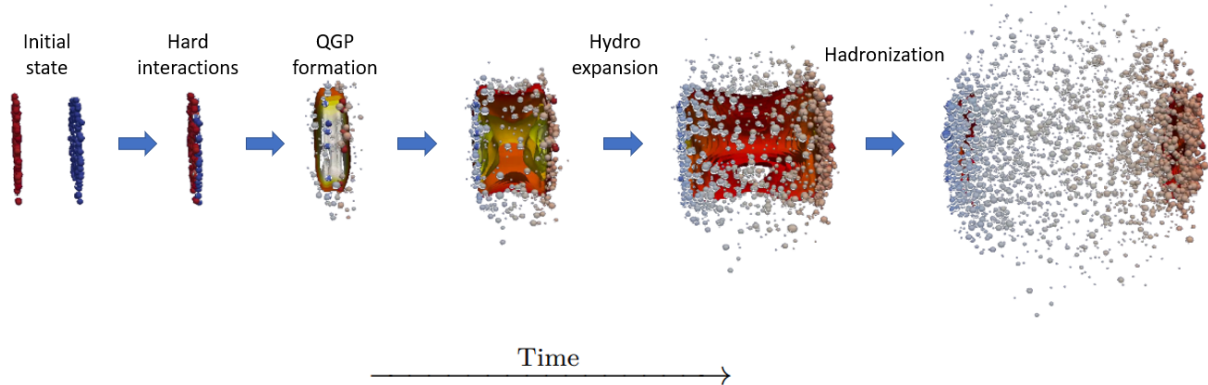


Figure 2.1: Stages of a heavy-ion collision. The initially Lorentz contracted nuclei accelerate at each other, yielding a hard collision and forming the Quark-Gluon Plasma. The medium then expands according to relativistic hydrodynamics up to a point where the quarks and gluons have enough energy to combine into hadrons and free-stream from the system [29].

our universe.

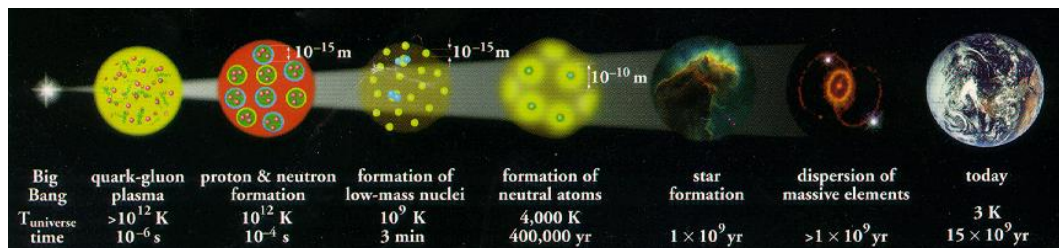


Figure 2.2: History of the universe [32]. We note that the Quark-Gluon Plasma is the first matter formed after  $10^{-6}$  s of the big bang, followed by the formation of protons, neutrons and low mass nuclei.

The main goal of heavy-ion collisions is to map the QCD phase diagram, shown in Fig. 2.3. This simplified diagram describes the phases of matter according to the standard model QCD theory, the hadron gas and the Quark-Gluon Plasma, as a function of temperature  $T$  and baryon chemical potential  $\mu_B$ . The baryon chemical potential express how much more quarks there are over antiquarks in the QCD matter -  $\mu_B$  equals zero implies equal number of quarks and antiquarks, a good approximation for the matter produced at the LHC and RHIC. Moreover, at vanishing baryon density, lattice calculations [33, 34] showed that the quark-hadron transition is a continuous crossover, possibly delimited by a critical end point (CEP) that separates the first order transition. Experiments like CERN SPS [35] and the RHIC Beam Energy Scan [36] explore the CEP [37] and the continuous cross-over between the QGP and the hadronic matter, but this is still not completely understood. In order to explore the rest of the diagram, where  $\mu_B$  is

non-zero, lower beam energies are required.

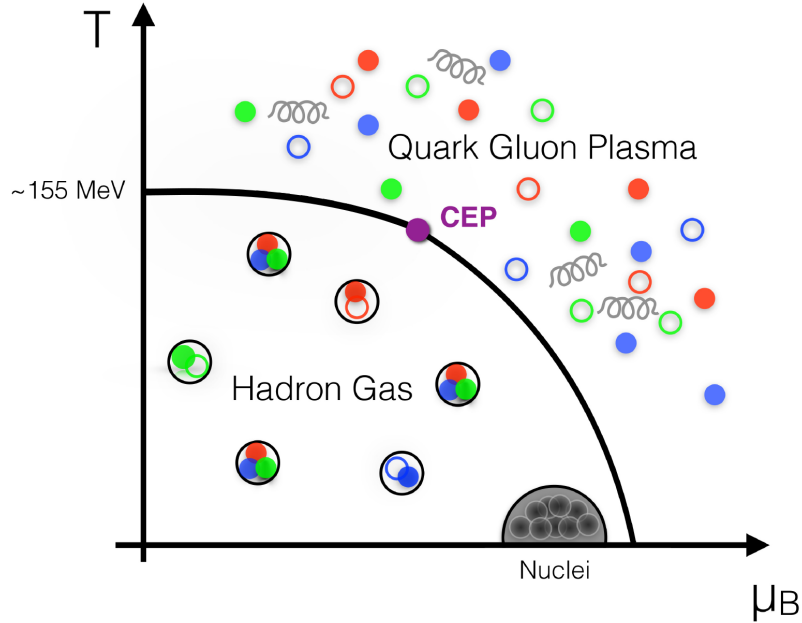


Figure 2.3: Phase diagram of the QCD matter in terms of the temperature  $T$  and the baryon potential  $\mu_B$ . The Quark-Gluon Plasma phase is separated from the hadronic matter by a phase transition. LHC and RHIC top energies, for example, explore the vanishing baryon potential, while lower energies reaches  $\mu_B > 0$  regions. The critical end point (CEP) represents a second order transition point that possibly marks the separation between the two different states. The location of the CEP is still an open question. Adapted from [38].

In this work we are mainly interested in a collision where energetic partons pairs are created and eventually form a structure of jet of hadrons, all happening within the region of formation of the QGP. This way, a dijet created inside this relativistic fluid will carry important information about the medium it travelled. Chapters 4 and 5 are dedicated to the study of a jet passing through the plasma and how it can be probed by analysing the final free-streaming particles. But before going in more detail about the core part of this work, we must first develop a better understanding of the heavy-ion collision framework and the formation of the Quark-Gluon Plasma.

## 2.1 Conventions and the Kinematic Variables

When talking about relativistic heavy-ion collisions and the description of physical properties of the Quark-Gluon Plasma, it's convenient to introduce the variables and conventions used in this framework. The kinematic variables are convenient in

a way that they present simple properties under a change of the frame of reference. For example, under a Lorentz transformation, the rapidity variable  $y$  and the pseudorapidity  $\eta$  have simpler properties than the relativistic velocity  $v$ . The Milne coordinates, for instance, replaces the usual coordinate system by a set of new variables, resulting in a simpler description of the relativistic hydrodynamic equations. We'll start reviewing the notation and conventions. Then, introduce the rapidity and pseudorapidity variables that link the Milne coordinates to the usual space-time coordinates.

### 2.1.1 Conventions

The space-time coordinates of a point  $x$  are denoted by a contravariant four-vector  $x^\mu$ ,

$$x^\mu = (x^0, x^x, x^y, x^z) = (t, \vec{x}) = (t, x, y, z). \quad (2.1)$$

The momentum four-vector is also a contravariant vector  $p^\mu$ , with components

$$p^\mu = (p^0, p^1, p^2, p^3) = (E, \vec{p}) = (E, p_x, p_y, p_z). \quad (2.2)$$

Note that we will use the natural units  $\hbar = c = 1$  throughout this work. The space-time metric tensor  $g_{\mu\nu}$  adopted is

$$g_{\mu\nu} = \begin{pmatrix} 1 & 0 & 0 & 0 \\ 0 & -1 & 0 & 0 \\ 0 & 0 & -1 & 0 \\ 0 & 0 & 0 & -1 \end{pmatrix}, \quad (2.3)$$

allowing the relation between the covariant vector  $x_\mu$  and the contravariant vector  $x^\mu$  to be written as

$$x_\mu \equiv (x_0, x_1, x_2, x_3) \equiv g_{\mu\nu} x^\nu = (t, -x, -y, -z). \quad (2.4)$$

We will be using the repeated index notation, implying a summation with respect to that index, unless stated otherwise. The scalar product of two four-vectors  $x$  and  $v$  is defined as

$$x \cdot v \equiv x^\mu v_\mu = g_{\mu\nu} x^\mu v^\nu = x^0 v^0 - \vec{x} \cdot \vec{v}. \quad (2.5)$$

Finally, the four-momentum operator in coordinate representation and the gradient operator  $\nabla$  are

$$\begin{aligned} p^\mu &= i\partial^\mu = (i\partial^t, i\partial^x, i\partial^y, i\partial^z) = ig^{\mu\nu} \partial_\nu, \\ p^\mu &= (i\partial_t, -i\partial_x, -i\partial_y, -i\partial_z), \\ p^\mu &= \left(i\frac{\partial}{\partial t}, -i\frac{\partial}{\partial x}, -i\frac{\partial}{\partial y}, -i\frac{\partial}{\partial z}\right), \end{aligned} \quad (2.6)$$

$$\begin{aligned} \nabla &= (\nabla_x, \nabla_y, \nabla_z) = (\partial_x, \partial_y, \partial_z), \\ &= (\partial/\partial x, \partial/\partial y, \partial/\partial z). \end{aligned} \quad (2.7)$$

### 2.1.2 Rapidity and Pseudorapidity

In the description of particles created in heavy-ion collisions, the rapidity is an important kinematic variable. Considering that the beam is in the  $z$  direction, also referred as the longitudinal direction, the Lorentz boost will be in the  $z$  direction. Then, the rapidity of a particle is defined in terms of the energy and momentum components  $E$  and  $p_z$ ,

$$y = \frac{1}{2} \ln \left( \frac{E + p_z}{E - p_z} \right). \quad (2.8)$$

By rewriting the energy and the momentum in the  $z$  direction in terms of the rest mass  $m$ ,

$$E = \gamma m, \quad (2.9)$$

$$p_z = \gamma \beta m, \quad (2.10)$$

where  $\beta = v$ , the rapidity takes the form

$$y_\beta = \frac{1}{2} \ln \left( \frac{1 + \beta}{1 - \beta} \right). \quad (2.11)$$

In the classical limit, the rapidity of a particle travelling in the  $z$  direction is equal to the longitudinal velocity of the particle. That can be checked by taking small values of  $\beta$  in Eq. (2.11) and expanding it in Taylor series, yielding

$$y_\beta = \beta + \mathcal{O}(\beta^2). \quad (2.12)$$

Therefore, for  $\beta \ll 1$ ,  $y_\beta = \beta$ .

It's also possible to draw a link between rapidity, energy and momentum in the  $z$  direction. First, we rewrite Eq. (2.8) as

$$e^y = \sqrt{\frac{E + p_z}{E - p_z}}, \quad (2.13)$$

and

$$e^{-y} = \sqrt{\frac{E - p_z}{E + p_z}}. \quad (2.14)$$

Adding Eqs. (2.13) and (2.14) yields

$$E = m_T \cosh y, \quad (2.15)$$

where  $m_T^2 = m^2 + p_T^2 = m^2 + p_x^2 + p_y^2$  is the transverse mass of the particle. Subtracting Eqs. (2.13) and (2.14) results in

$$p_z = m_T \sinh y. \quad (2.16)$$

Due to Eqs. (2.16) and (2.15), it's possible to use the rapidity to compute important properties of the particles, such as its energy and longitudinal momentum. Then, in order to complete the kinematics information of a particle, we are only left to compute the transverse momentum in the  $xy$  plane, the  $p_T$ . Moreover, the rapidity has a particular property that makes it a special variable. The value  $y$  in a frame of reference  $A$  is related to the value of  $y'$  in a Lorentz frame of reference  $A'$  by a simple additive constant:

$$y' = y - y_\beta, \quad (2.17)$$

where  $y_\beta$  is defined in Eq. (2.11). In summary, the two main properties of the rapidity given by Eqs. (2.12) and (2.17) makes it behave as a relativistic analog of the velocity in the longitudinal direction of the particle.

Different from the rapidity, that needs a measure of energy or momentum to be calculated, the pseudorapidity  $\eta$  can be computed using the angle of the detected particle relative to the longitudinal direction:

$$\eta = -\ln[\tan(\theta/2)]. \quad (2.18)$$

We can also write the pseudorapidity in terms of the particle momentum  $p$

$$\eta = \frac{1}{2} \ln \left( \frac{|p| + p_z}{|p| - p_z} \right). \quad (2.19)$$

The last equation enables a straightforward relation between the rapidity and pseudorapidity variables - for relativistic particles (large momentum),  $|p| \approx E$ , and  $\eta \approx y$ . Pseudorapidity is, therefore, more useful when analysing ultra-relativistic particles from hadron collider. Not only the particle interaction does not need to be aligned with the center of mass frame of the detectors, it's much easier to estimate  $\eta$  based on the angle measured, then  $y$  based on the momentum and energy.

## 2.2 Stages of a Collision

The study of the thermodynamic and transport properties of the QGP is not a straightforward task. Experimentally, we can only measure the energy and momenta of the particles produced in the final stage of the collision, when quarks and gluons combine to form hadrons. In order to investigate the properties of the plasma, the entire heavy-ion collision process needs to be modeled. The model starts considering a beam of particles travelling in the  $z$  direction. The two relativistic nuclei, shaped like flat discs due to Lorentz contraction, pass through each other, leaving a path of energetic particles in the interaction region. Figure 2.4 illustrates the system before and after the collision. The impact parameter limits the degree of interaction between the two nuclei. The smaller b

is, the more participants interact in the collision and the more particles are created. The result is a volume of hot and dense matter that might form the QGP, depending on the energy deposited.

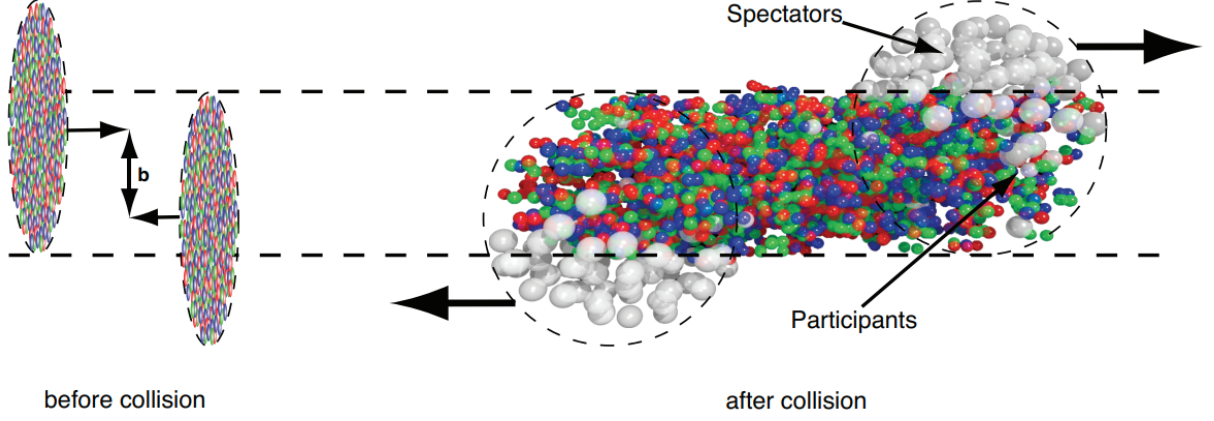


Figure 2.4: Illustration of a collision between two heavy nuclei in relativistic energies, with impact parameter  $\mathbf{b}$  and subsequent interactions [39].

In order to better describe the physical processes in a heavy-ion collision, it's usual to express the quantities in the Milne coordinate system rather than in the Cartesian one. This is useful when the system is symmetric under a Lorentz boost, which is the case we are dealing with. The main modification lies in the substitution of the  $(z, t)$  plane by the  $(\tau, \eta_s)$  plane. For a boost in the  $z$  direction, we define

$$\tau = \sqrt{t^2 - z^2}, \quad (2.20)$$

$$\eta_s = \frac{1}{2} \ln \left( \frac{t + z}{t - z} \right), \quad (2.21)$$

where  $\tau$  is called the proper time of a particle with constant velocity in the  $z$  direction and  $\eta_s$  is the spatial-rapidity. This name comes from its resemblance to the usual rapidity, but with the momentum components replaced by the position.

We are able to display the space-time evolution of a particle in both coordinate systems  $(z, t)$  and  $(\tau, \eta_s)$  by drawing the light-cone diagram. Figure 2.5 shows the contours of constant proper time, represented by the hyperbolas, and the contours of constant rapidity, represented by the two  $45^\circ$  lines, delimiting the rapidity values of  $y = \pm\infty$ . Eqs. (2.20) and (2.21) restricts the possible positions inside the light-cone. If, for instance,  $|t| < |z|$ ,  $\eta_s$  and  $\tau$  become complex numbers, which is beyond our domain. Also, the

$t < 0$  region of the cone is neglected, since it leads to negative values of logarithm in the spatial-rapidity expression. Hence, only the  $t > 0$  region should be regarded. We can also write the space-time coordinates in terms of the light-cone variables. Their expressions take the form

$$t = \tau \cosh \eta_s \tag{2.22}$$

$$z = \tau \sinh \eta_s. \tag{2.23}$$

The space-time evolution of the collision, which illustrates the stages of the scenario shown in Fig. 2.4, is described by the Bjorken model [40]. Within this model, the collision can be divided into the pre-equilibrium phase, the relativistic fluid evolution, and the freeze-out phase. In Fig. 2.5 we show these stages of a heavy-ion collision, where the pre-equilibrium phase is represented by the initial gray area, the fluid QGP evolution by the orange, and the final hadronic stage by blue. During the hadronic stage, the first hyperbolic curve corresponds to the chemical freeze-out time. The final boundary of the blue region corresponds to the kinetic freeze-out after which the particles no longer interact. The pre-equilibrium phase provides the initial conditions for the relativistic fluid evolution, modelling the spatial distribution of the energy and pressure deposition. It's often described by geometric models such as Glauber Monte-Carlo approaches [41], in which the underlying strong interactions are encapsulated in the inelastic nucleon-nucleon cross-section. In the initial condition, a mass of hot and dense matter is formed at  $\tau_0 < 1$  fm/c and is thermalized around  $\tau = 1$  fm/c, where the QGP is formed. At this time, the fireball expands due to thermal pressure created by the local temperature. The bulk evolution is then described by relativistic viscous hydrodynamics. At this point, it's fair to say that the QGP behaves nearly like a perfect fluid, with almost no viscosity. Due to the initial high pressure, the QGP continues to expand until it reaches the phase transition temperature of approximately  $T_{Ch} = 150$  MeV, which delimits the beginning of the hadronic phase. Hadrons keep interacting, and while the energy is sufficient, inelastic collisions will keep changing the chemical composition of the system. After some time, the inelastic collisions will cease and the chemical composition will freeze-out.

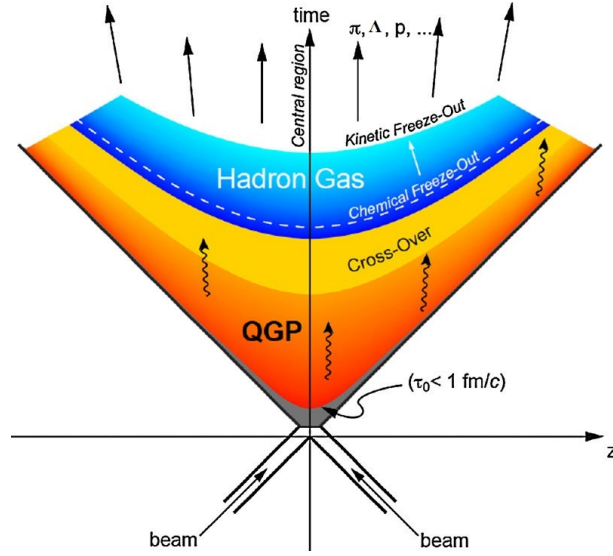


Figure 2.5: Space-time evolution of an ultra-relativistic heavy-ion collision. As the two beams collide, the matter formed goes through the pre-equilibrium phase, the QGP evolution, hadron gas and finally kinetic freeze-out, where the particle free-stream from the system. The yellow area represents the cross-over region, dividing the QGP from the hadronic matter. Adapted from [42].

Finally, as the system continues to cool down, it reaches the kinetic freeze-out phase where both inelastic and elastic collisions stop and the particles free-stream from the collision. In this work, we model the stages of the collision in a simulation chain. The initial condition of the two nuclei colliding, the hydrodynamic evolution of the QGP and the creation of the final particles are the main steps taken in order to describe our physical system. More details about the physical models used in this work will be covered in Chapter 4. Now, in the next Chapter, we describe the theoretical framework in which the Quark-Gluon Plasma is modeled.

---

# Relativistic Hydrodynamics and Vorticity in the Quark-Gluon Plasma

---

The concept of describing the expansion of a strongly interacting matter formed in high-energy collisions through ideal hydrodynamics was first introduced by Landau, in 1953 [43]. At the time, it wasn't clear that this dense system produced by a highly energetic collision could be described by a hydrodynamic theory. Later, in the early 2000s, experimental results from the the Relativistic Heavy Ion Collider (RHIC) [6, 44, 45], at Brookhaven National Laboratory, showed evidence towards the description of QGP medium expansion using hydrodynamic solutions. The solutions from ideal hydrodynamic equations were, at first, effective in describing the flow dynamics of the medium. As the heavy-ion experiments evolved, the bigger precision of data allowed a more detailed analysis of the collision, and a viscous hydrodynamic description of the QGP came into play describing the system evolution with dissipative effects, such as bulk and shear viscosity.

In the next sections we will present a summary with some key points of the hydrodynamical theory, starting with the basic concepts of the non-viscous classical hydrodynamics and build our way up to the viscous relativistic hydrodynamics.

## 3.1 Non-relativistic Hydrodynamics

The non-relativistic hydrodynamic theory describes the evolution of the fluid we observe in our daily life, such as the flow of water in the sink, or the ripples caused by a rain drop in a pond. The dynamics of such a liquid can be defined in terms of its degrees of freedom: the fluid velocity  $\mathbf{v}(t, \mathbf{x})$ , pressure  $P(t, \mathbf{x})$  and mass density  $\rho_m(t, \mathbf{x})$ .

These three quantities are linked by the fluid dynamics equations [46, 47],

$$\rho_m \partial_t \mathbf{v} + \rho_m (\mathbf{v} \cdot \nabla) \mathbf{v} = -\nabla P \quad (3.1)$$

$$\partial_t \rho_m = -\nabla(\rho_m \mathbf{v}). \quad (3.2)$$

Equations (3.1) and (3.2) are commonly referred as the Euler equation and Continuity equation, and are valid for ideal fluids. Since there are three variables and only two equations, the complete solution is usually accomplished with an equation of state, such as  $P = P(\rho_m)$ .

For the non-ideal case, the Euler equations can be generalized to the Navier-Stokes equation [48, 49],

$$\frac{\partial v^i}{\partial t} + v^k \frac{\partial v^i}{\partial x^k} = -\frac{1}{\rho_m} \frac{\partial P}{\partial x^i} - \frac{1}{P} \frac{\partial \Pi^{ki}}{\partial x^k}, \quad (3.3)$$

$$\Pi^{ki} = -\eta \left( \frac{\partial v^i}{\partial x^k} + \frac{\partial v^k}{\partial x^i} - \frac{2}{3} \delta^{ki} \frac{\partial v^l}{\partial x^l} \right) - \zeta \delta^{ik} \frac{\partial v^l}{\partial x^l}, \quad (3.4)$$

where the indices represent the three spacial directions. The quantity  $\Pi^{ki}$ , called viscous stress tensor, carries information about the shear viscosity  $\eta$  and the bulk viscosity  $\zeta$ . These two coefficients constitute important dissipative properties of a viscous fluid. The shear viscosity is caused by the relative motion of adjacent fluid cells - the faster moving fluid will transfer part of its momentum to the slower fluid, generating a momentum gradient that will slow down the fluid's movement. Correspondingly, the bulk viscosity is a property that depends on the temperature and pressure of the fluid. It is the resistance to expansion and compression motions of the medium. Therefore, the classical non-relativistic Navier-Stokes equation can be applicable to describe many viscous systems, and the relativistic hydrodynamic equations should, in the classical regime, be reduced to it.

For completeness, let us consider the conservation of energy in an ideal fluid element. We begin by noting that the total time derivative of the energy can be written as the total energy flux through a surface plus the work done by external forces and adjacent fluid elements. The total energy density  $E$ , for instance, is the sum of the kinetic energy

density and the internal energy of the fluid element,

$$E = \frac{\rho_m \mathbf{v}^2}{2} + \epsilon_{int}. \quad (3.5)$$

Thus, the equation of conservation of energy reads

$$\partial_t \left( \rho_m + \frac{\rho_m}{2} \beta^2 + \epsilon_{int} \right) + \nabla \cdot \beta \left( \rho_m + \frac{\rho_m}{2} \beta^2 + \epsilon_{int} + P \right) = 0, \quad (3.6)$$

where  $\rho_m$  is the rest mass of the fluid and  $\beta = \mathbf{v}$ . We can write a ‘‘covariant like’’ expression that combines both Eqs. (3.1) and (3.6),

$$\partial_\mu T_{classic}^{\mu\nu} = 0, \quad (3.7)$$

$$T_{classic}^{\mu\nu} = \begin{pmatrix} \rho_m + \rho_m \beta^2/2 + \epsilon_{int} & \rho_m \beta^T \\ (\rho_m + \rho_m \beta^2/2 + \epsilon_{int} + P)\beta & \rho_m \beta \beta^T + P \mathbb{1} \end{pmatrix}, \quad (3.8)$$

where  $\beta^T$  is the transpose component of  $\beta$ . Even though the expressions above look like relativistic equations, the tensor  $T_{classic}^{\mu\nu}$  is not covariant under a Lorentz transformation. In the next section we will approach the relativistic hydrodynamic equation, discussing the proper covariant energy-momentum tensor.

## 3.2 Relativistic ideal hydrodynamics

In this section we will discuss the relativistic hydrodynamic equations through mathematical and physical considerations of the energy-momentum tensor. We begin by analysing the possible hydrodynamic variables in Eq. (3.8) that can be related to the relativistic  $T^{\mu\nu}$ . At first sight, we can rule out the scalar quantities such as the local pressure  $P$  and the total energy density  $\rho_m + \rho_m \beta^2/2 + \epsilon_{int}$ , since they cannot be written in a covariant form. We are left with two possible quantities, the velocity vector  $\mathbf{v}$ , that can be extended to the four-velocity  $u^\mu$ , with normalization  $u^\mu u_\mu = 1$ , and the metric tensor  $g^{\mu\nu}$ . Both can be used in the construction of the relativistic energy-momentum tensor, yielding the general form

$$T^{\mu\nu} = Au^\mu u^\nu + Bg^{\mu\nu}, \quad (3.9)$$

where  $A$  and  $B$  are scalar functions. By finding these scalar functions and applying the conservation law in Eq. (3.7), we are able to find the relativistic equations. The first step is to compute  $T^{\mu\nu}$  in a local rest frame (LRF), where  $u^\mu = (1, 0, 0, 0)$ . This leads to

$$T_{LRF}^{\mu\nu} = \begin{pmatrix} A + B & 0 \\ 0 & -B\mathbb{1} \end{pmatrix}. \quad (3.10)$$

The energy density  $\epsilon$ , represented by the component  $T^{00}$  of the tensor [50], can then be written as

$$T_{LRF}^{00} = A + B = \epsilon. \quad (3.11)$$

In addition, by making  $\beta = 0$  in Eq. (3.8), we can compare  $T_{LRF}^{\mu\nu}$  to  $T_{classic}^{\mu\nu}$  and interpret the scalar quantity  $-B$  as the thermodynamic pressure  $P$  in the local rest frame. Therefore, with this association, we can write the relativistic energy-momentum tensor as

$$T_{ideal}^{\mu\nu} = (\epsilon + P)u^\mu u^\nu - Pg^{\mu\nu}. \quad (3.12)$$

In a general reference frame, the four-velocity takes the form  $u^\mu \rightarrow (\gamma, \gamma\beta)$ , and the tensor can be written in a contracted  $2 \times 2$  matrix as

$$T_{ideal}^{\mu\nu} = \begin{pmatrix} (\epsilon + P)\gamma^2 - P & (\epsilon + P)\gamma^2\beta^T \\ (\epsilon + P)\gamma^2\beta & (\epsilon + P)\gamma^2\beta\beta^T + P\mathbb{1} \end{pmatrix}, \quad (3.13)$$

where  $\gamma$  is the usual Lorentz factor. For completeness, the  $4 \times 4$  form of  $T_{ideal}^{\mu\nu}$  is

$$T_{ideal}^{\mu\nu} = \begin{pmatrix} (\epsilon + P)\gamma^2 - P & (\epsilon + P)\gamma^2 v_x & (\epsilon + P)\gamma^2 v_y & (\epsilon + P)\gamma^2 v_z \\ (\epsilon + P)\gamma^2 v_x & (\epsilon + P)\gamma^2 v_x^2 + P & (\epsilon + P)\gamma^2 v_x v_y & (\epsilon + P)\gamma^2 v_x v_z \\ (\epsilon + P)\gamma^2 v_y & (\epsilon + P)\gamma^2 v_y v_x & (\epsilon + P)\gamma^2 v_y^2 + P & (\epsilon + P)\gamma^2 v_y v_z \\ (\epsilon + P)\gamma^2 v_z & (\epsilon + P)\gamma^2 v_z v_x & (\epsilon + P)\gamma^2 v_z v_y & (\epsilon + P)\gamma^2 v_z^2 + P \end{pmatrix}. \quad (3.14)$$

Now that we have an expression for  $T^{\mu\nu}$ , we can use the energy-momentum conservation equation

$$\partial_\nu T^{\mu\nu} = 0 \quad (3.15)$$

to obtain the relativistic equations. Therefore, the equations of movement are

$$D\epsilon + (\epsilon + P)\partial_\mu u^\mu = 0 \quad (3.16)$$

$$(\epsilon + P)Du^\alpha - \nabla^\alpha P = 0, \quad (3.17)$$

where  $D \equiv u^\alpha \partial_\alpha$  is the comoving time derivative and  $\nabla^\mu \equiv (g^{\mu\nu} - u^\mu u^\nu) \partial_\alpha$  is the spacial projected derivative. These are the fundamental equations for a relativistic ideal fluid. In the non-relativistic regime,  $D$  and  $\nabla^\alpha$  are reduced to time and space derivatives. To obtain the classic equations back, we can consider the energy density to be mostly dominated by the mass density  $\rho_m$ , and the pressure to be negligible compared to the energy ( $\epsilon \gg P$ ). Thus, applying these constrains to the relativistic equations, we recover the classical Continuity (3.2) and Euler (3.1) equations.

### 3.3 Relativistic Viscous Hydrodynamics

So far, in the ideal framework, all dissipative effects have been, by definition, neglected. If we are interested in describing the viscous effects caused by a non-ideal flow, the usual energy-momentum tensor, derived in Eq. (3.12), will have to take into account other effects, such as bulk and shear viscosity. As a first approach, we can write the energy-momentum tensor as a sum of two quantities, an ideal part and a viscous part,

$$T^{\mu\nu}_{visc} = T^{\mu\nu}_{ideal} + \Pi^{\mu\nu}, \quad (3.18)$$

where  $T^{\mu\nu}_{ideal}$  is given by Eq. (3.12) and  $\Pi^{\mu\nu}$  is the viscous stress tensor. Through the energy-momentum conservation equation, now applied to Eq. (3.18), the dynamics equations obtained are

$$D\epsilon + (\epsilon + P)\partial_\mu u^\mu - \frac{1}{2}\Pi^{\mu\nu}(\nabla_\mu u_\nu + \nabla_\nu u_\mu) = 0, \quad (3.19)$$

$$(\epsilon + P)Du^\alpha - \nabla^\alpha P + \Delta^\alpha_\nu \partial_\mu \Pi^{\mu\nu} = 0, \quad (3.20)$$

where the expressions for the viscous stress tensor  $\Pi^{\mu\nu}$  is written in terms of the shear stress tensor  $\pi^{\mu\nu}$  and a bulk pressure  $\Pi$ . Mathematically,

$$\Pi^{\mu\nu} = \pi^{\mu\nu} + \Delta^{\mu\nu}\Pi, \quad (3.21)$$

where  $\Pi = -\xi\partial_\mu u^\mu$  and  $\pi^{\mu\nu} = \eta(\Delta^{\mu\alpha}\Delta^{\nu\beta} + \Delta^{\nu\alpha}\Delta^{\mu\beta} - \frac{2}{3}\Delta^{\nu\alpha}\Delta^{\mu\beta})\partial_\alpha u_\beta$  and  $\Delta^{\mu\nu} = g^{\mu\nu} - u^\mu u^\nu$ . We note that these quantities are directly related to the shear viscosity coefficient  $\eta$  and the bulk viscosity coefficient  $\xi$ . Reorganizing Eqs. (3.19) and (3.20), the shear viscosity can be combined into  $\eta/(\epsilon + P) = \eta/(Ts)$ , where the dimensionless ratio of viscosity to entropy density  $s$  is called specific viscosity - it controls how fast the shear stress of the fluid is dissipated into heat. So, the higher it is, the more heat is generated within the fluid. The value of  $\eta/s$  was calculated for strongly-coupled system using AdS/CFT methods, indicating a limiting value of  $\eta/s = 1/4\pi$  [51]. This threshold limit for the specific viscosity then inspired further studies aiming the determination of the  $\eta/s$  of the QGP, where it was found to be in the range  $0.07 \leq \eta/s \leq 0.43$  [52]. Further studies of the effects of the bulk and shear viscosities on the flow dynamics of a heavy-ion collision can be found in Refs. [53–56].

### 3.4 Vorticity and Polarization in the QGP

Now we turn our attention to the main hydrodynamic effect studied in this work, the vorticity caused by a jet thermalization in the Quark-Gluon Plasma, and its connection to the polarization of  $\Lambda$  particles. We begin with a description of the global polarization and the importance of the  $\Lambda$  hyperon in this measurement. Next we cover the momentum-dependent “local” polarization, the concept of polarization used to link the vorticity of the QGP and the spin of the particle that comes out of the freeze-out hypersurface. This will be our main observable analysed throughout this work.

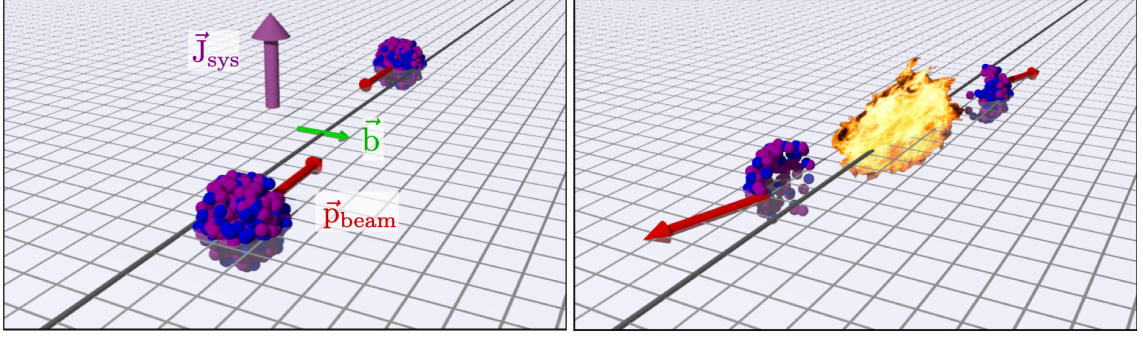


Figure 3.1: Sketch of a collision and the formation of the fireball with total angular momentum represented by  $\hat{J}_{sys}$ . The left Fig. represents the two nuclei before the collision, with impact parameter  $\vec{b}$ , momentum of the beam  $\vec{p}_{beam}$  and momentum of the collision  $\hat{J}_{sys} = \vec{b} \times \vec{p}_{beam}$ . The right Fig. shows the formation of the fireball. In a non-central collision, this fireball will develop an angular momentum, and consequently, vorticity in the direction of the total angular momentum  $\hat{J}_{sys}$  [25].

### 3.4.1 Global Polarization and the Importance of the Lambda Particle

When we talk about vorticity effects in a fluid, we picture common situations in which a fluid like water swirls or forms an eddy. In both these situations, the angular momentum is the main cause of the effect. In general, we can state that the application of angular momentum to any fluid is bound to be accompanied by a vortical effect. This effect is also present in the context of high-energy collisions, more specifically in the fluid behavior of the Quark-Gluon Plasma. In this case, the overlapping region of the two colliding nuclei, when the collision is not precisely head-on, can generate a great amount of angular momentum due to the spinning movement of the fireball. The resulting particles formed from the blast will then suffer a small deflection that, upon physical measurement, allows the determination of the angular momentum of the whole system,  $\hat{J}_{sys}$  [57, 58]. Figure 3.1 shows a sketch of a collision and the formation of the Quark-Gluon Plasma; the non-interacting fragments are called spectators and are depicted on the right side as the two intact parts of the nucleus travelling with opposite momentum. In this scenario, we can define the total angular momentum plane as the cross product between the impact parameter  $\vec{b}$  and the momentum of the beam  $\vec{p}_{beam}$ , that is,  $\hat{J}_{sys} = \vec{b} \times \vec{p}_{beam}$ . Due to the high gradients of velocity formed by almond shaped region of overlapping nuclei, vorticity will also be formed and will point to the same direction as  $\hat{J}_{sys}$ .

The spinning motion of the fluid can generate a spin alignment, or polarization, of the final particles. When averaged over the entire system, the resultant polarization

of these particles will be parallel to the fireball's angular momentum, denoted as  $\vec{J}_{QGP}$ , and consequently, to  $\vec{J}_{sys}$ . This measurement is called global hyperon<sup>1</sup> polarization, since it involves an average polarization of hyperons. It is observed, for example, in Au–Au collisions with center of mass energy  $\sqrt{s_{NN}} = 200$  GeV, as measured by the STAR experiment, at RHIC [59]. Since the entire bulk of QGP is spinning, it's natural to expect that all hadrons with spin created after the freeze-out will be polarized.

The particles created in the collision are measured using detectors mounted around the collision point. Most of the collider experiments have a tracking type detector that is capable of measuring the momentum of the produced particles through the reconstruction of the track left by charged particles in a medium. For example, in a time projection chamber (TPC) type detector [60], a charged particle traverses a large volume of gas, leaving a ionized track that provides a 3D picture of the particle trajectory, from which we can calculate not only the momentum, but also infer the particle type through the amount of energy deposited ( $dE/dx$ ). Often, TPC tracking detectors are coupled to time-of-flight (ToF) detectors [61] that improves particle identification through the determination of the velocity and the mass of the particles. Some neutral particles that cannot be measured directly since they do not create a ionizing track, can still be measured through the reconstruction of the charged tracks left by the daughter tracks of the decay. For example, a Lambda hyperon that is a neutral particle, hence not measurable in the TPC, will decay into a proton and a pion that will leave a measurable track in the TPC. By energy and momentum conservation, it is possible to reconstruct and obtain the momentum of the original Lambda particle.

In this context, we are mainly interested in determining the hadron polarization by looking at the charged particles it decays into. More specifically, we analyse weak parity-violating hyperons, which have the characteristics of having daughter baryons being emitted in its original spin direction. This property comes in handy since we know we can get important information of polarization of hyperons just by looking at its byproducts. Hyperon candidates for the polarization measurement can be, for example,  $\Xi^+$ ,  $\Xi^-$ , reconstructed by the decays  $\Xi^+ \rightarrow \Lambda + \pi^+$  and  $\Xi^- \rightarrow \bar{\Lambda} + \pi^-$ ,  $\Lambda$  and  $\bar{\Lambda}$ , reconstructed by proton (anti-proton) and pion decays,  $\Lambda \rightarrow p + \pi^-$  and  $\bar{\Lambda} \rightarrow \bar{p} + \pi^+$ . A comparison between the polarization of  $\Lambda$ 's and  $\Xi$ 's can be found in Ref. [62].

---

<sup>1</sup>Hyperon is a particle made up of three quarks, with at least one being strange quark. The others may be up or down quarks.

In general,  $\Lambda$  is more straightforward hyperon to be analysed and identified. The daughter proton tends to be emitted along its polarization direction and it has only one decaying vertex, while, for example,  $\Xi$ 's have two [63]. Figure 3.2 shows the reconstructed tracks of the particles at the STAR TPC, measured in a Au–Au collision. In red we can see the tracks left by the decay of a  $\Lambda$  particle in pion and proton, as well as a peak of the  $\Lambda$  mass in the invariant mass distribution plot. Secondary  $\Lambda$ 's, coming from the decays of  $\Sigma^0$ ,  $\Sigma^*$  or  $\Xi$  for example, also carries the polarization of the parent particle and represent a considerable fraction of the measured  $\Lambda$  particles by the detector [25]. Nevertheless, it was shown [64, 65] that this secondary  $\Lambda$  polarization is almost the same as the primary  $\Lambda$ 's. In this sense, the following discussion is based on the primary Lambdas, that is,  $\Lambda$ 's emitted from the freeze-out hypersurface. The relation between the

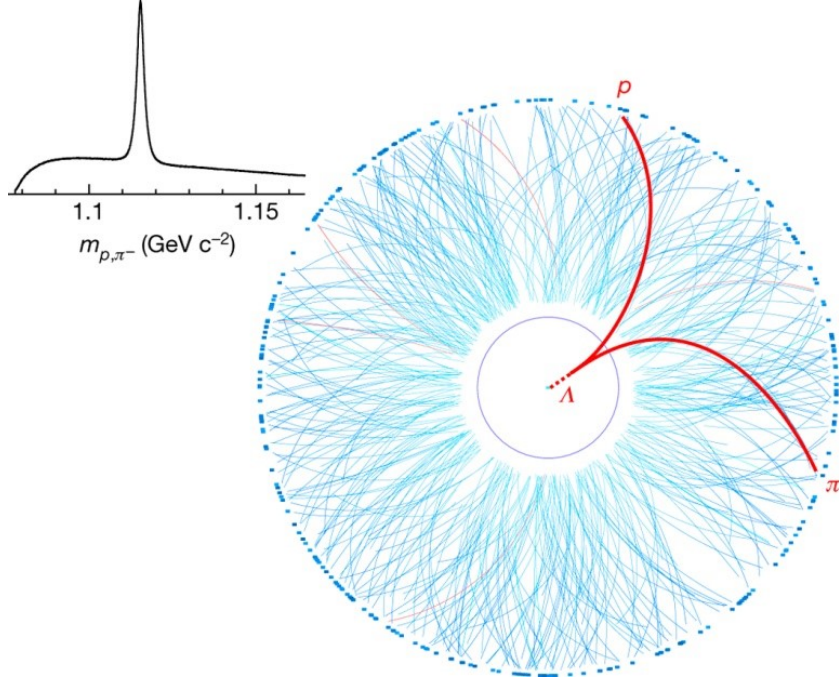


Figure 3.2: Star TPC reconstruction of a Au–Au collision. Particles reconstructed tracks are shown as the curved colored lines. The weak decay of  $\Lambda$  into  $p$  and  $\pi$  is shown in red. The paths are reconstructed based on charged particles' time of flight and ionization left on the TPC. The invariant mass distribution is also shown, indicating a peak at the  $\Lambda$  mass, that is, around 1115 MeV [3] .

angular distribution of the daughter proton and the  $\Lambda$  polarization,  $\vec{P}_\Lambda$ , is given by the equation [66]

$$\frac{dN_{proton}}{d \cos \theta} = \frac{1}{2} \left( 1 + \alpha_H \vec{P}_\Lambda \cdot \cos \theta \right), \quad (3.22)$$

where  $\alpha_H$  is the decay parameter, dependent on the hyperon species [67], and  $\theta$  is the angle between the daughter proton momentum and the polarization of the hyperon in its rest frame. Even though Eq. (3.22) establishes a direct connection between the proton and the polarization of the parent hyperon, the limited statistics of such events makes the exploration of this relation a hard task [3, 68]; an alternative is to look at the average polarization of  $\Lambda$ , a quantity we know that, by symmetry, will be parallel to the system angular momentum  $\vec{J}_{sys}$ . Therefore, the average projection of the polarization in the  $\vec{J}_{sys}$  direction is given by [3]

$$\bar{P}_\Lambda \equiv \langle \vec{P}_\Lambda \cdot \vec{J}_{sys} \rangle = \frac{8}{\pi\alpha_H} \frac{\langle \cos(\phi_p - \phi_{\vec{J}_{sys}}) \rangle}{R_{EP}}, \quad (3.23)$$

where  $\phi_p$  is the azimuthal angle between the proton momentum and  $\vec{b}$ ,  $\phi_{\vec{J}_{sys}}$  the azimuthal angle of the total angular momentum<sup>2</sup>, and  $R_{EP}$  a correction factor that accounts for the resolution of  $\phi_{\vec{J}_{sys}}$  [69, 70]. The  $R_{EP}$  parameter carries the centrality dependency of the polarization. Figure 3.3 shows the values of the average polarization of  $\Lambda$  and  $\bar{\Lambda}$  for different values of collision centrality measured by the STAR experiment at RHIC; as one can intuitively expect, the less the two nuclei overlap, the more angular momentum is deposited in the fireball, yielding a bigger polarization.

### 3.4.2 Local Polarization and Vorticity

So far we've gone over the general concepts of global polarization of hyperons. To be exact, the polarization integrated over all  $\Lambda$  particles and dependent of a specific plane of event. But, as mentioned before, the high gradients of velocity formed by the collision of the nuclei generate not only polarization of particles, but also vorticity gradients in the Quark-Gluon Plasma. The polarization formed by the variations of fluid vorticity and space-momentum are usually called local polarization, or momentum-differential polarization. As such, in this work we are mainly interested analyzing the local polarization of the  $\Lambda$  particle as a response to the vorticity created inside the QGP. In particular, the vorticity created by a jet passing through the QGP.

Differently from the classical hydrodynamics, where the vorticity is the curl of the velocity field, in the relativistic hydrodynamics framework it can have many def-

<sup>2</sup>The anisotropy of the particles emission is used to compute the angle of the total angular momentum, also known as the event plane angle [69].

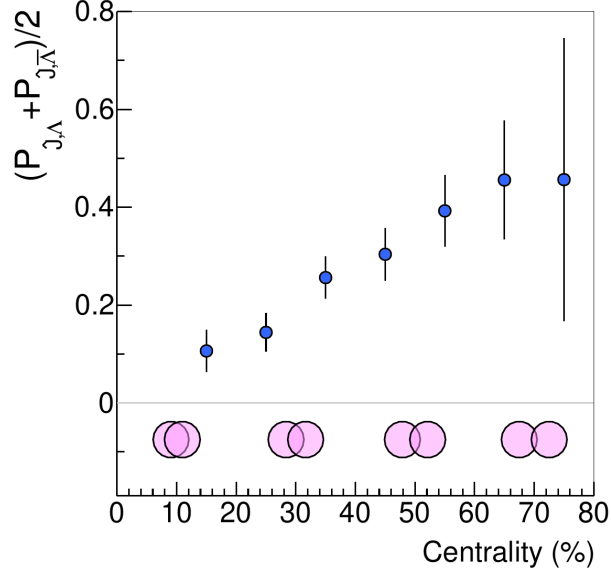


Figure 3.3: Average polarization of  $\Lambda$  and  $\bar{\Lambda}$  as a function of centrality, measured in a Au–Au collision with center of mass energy of 200 GeV, with decay parameter  $\alpha_H = 0.75$  measured by the STAR experiment at RHIC. We note that the value of polarization is inversely proportional to the centrality of the collision. Adapted from [25].

initions. Before discussing the polarization relation, let's first talk about these different types of vorticity. The kinematical vorticity is defined in terms of the four-velocity field  $w^\mu$ , being the intuitive relativistic version of the classical vorticity,

$$\omega_{kin}^{\mu\nu} = \frac{1}{2}(\partial^\nu u^\mu - \partial^\mu u^\nu). \quad (3.24)$$

The T-vorticity is useful when the temperature is the only independent thermodynamic variable, describing the vorticity generated by the temperature gradients,

$$\Omega^{\mu\nu} = \frac{1}{2}[\partial^\nu(Tu^\mu) - \partial^\mu(Tu^\nu)]. \quad (3.25)$$

The spacially projected kinetic vorticity replaces the usual derivative  $\partial_\nu$  in Eq. (3.24) by the spacial projected derivative  $\nabla^\mu = (g^{\mu\alpha} - u^\mu u^\alpha)\partial_\alpha$ , removing the acceleration components of the vorticity,

$$\omega_{SP}^{\mu\nu} = \frac{1}{2}(\nabla^\nu u^\mu - \nabla^\mu u^\nu). \quad (3.26)$$

These acceleration components appear when we open Eq. (3.26), resulting in

$$\omega_{SP}^{\mu\nu} = \frac{1}{2}(\partial^\nu u^\mu - \partial^\mu u^\nu) - \frac{1}{2}(u^\nu Du^\mu - u^\mu Du^\nu), \quad (3.27)$$

where  $D$  is the comoving time derivative, describing the covariant form of the time derivative evaluated with respect to the proper time  $\tau$ . Comparing Eq. (3.27) to Eq. (3.24) we confirm that the kinetic vorticity tensor with spacial projection subtracts the local acceleration from the usual kinetic vorticity. Finally, the thermal vorticity is defined in terms of the temperature  $T$ ,

$$\omega_{\mu\nu}^{th} = \frac{1}{2T}(\partial_\nu u_\mu - \partial_\mu u_\nu). \quad (3.28)$$

The main advantage of the thermal vorticity is that it's thought to be the one responsible for the polarization of particles in the QGP. Throughout Chapter 5 we'll be mostly interested in the consequences of the jet thermalization directly generating the thermal vorticity. There, we will use the following definition of the vorticity vector (based on the Pauli–Lubanski pseudovector for spin states of moving particles)

$$\omega^\mu \equiv \epsilon^{\mu\nu\rho\epsilon} u_\nu \omega_{\rho\epsilon}^{th}. \quad (3.29)$$

For spin-1/2 particles, the polarization is defined [25] as a function of  $w_{\mu\nu}^{th}$ ,

$$P^\mu(p) = -\frac{1}{8m} \epsilon^{\mu\rho\sigma\tau} p_\tau \frac{\int d\Sigma_\lambda p^\lambda n_F (1 - n_F) \omega_{\rho\sigma}^{th}}{\int d\Sigma_\lambda p^\lambda n_F}, \quad (3.30)$$

$$n_F = \frac{1}{1 + \exp(\beta^\mu p_\mu - \mu Q/T)}, \quad (3.31)$$

where  $n_F$  is the Fermi-Dirac-Juttner distribution,  $\mu$  is the chemical potential and  $Q$  is the generic charge [71]. In our calculations, we will not consider baryon currents, since we are dealing with LHC energies, where  $\mu = 0$  MeV is a very good approximation for the matter formed in a collision. The integral in Eq. (3.30) is done over the hypersurface  $\Sigma_\mu$ , and  $\epsilon^{\mu\rho\sigma\tau}$  is the Levi-Civita tensor, with  $\epsilon^{txyz} = 1$ . Using the metric  $g = (1, -1, -1, -1)^T$ , the four components of the polarization take the form:

$$P^t(p) = -\frac{1}{8m \int d\Sigma_\lambda p^\lambda n_F} \int d\Sigma_\lambda p^\lambda 2n_F(1 - n_F)(-\omega^{xy}p^x + \omega^{xz}p^y - \omega^{xy}p^z), \quad (3.32)$$

$$P^x(p) = -\frac{1}{8m \int d\Sigma_\lambda p^\lambda n_F} \int d\Sigma_\lambda p^\lambda 2n_F(1 - n_F)(-\omega^{ty}p^z + \omega^{tz}p^y - \omega^{yz}p^t), \quad (3.33)$$

$$P^y(p) = -\frac{1}{8m \int d\Sigma_\lambda p^\lambda n_F} \int d\Sigma_\lambda p^\lambda 2n_F(1 - n_F)(-\omega^{tz}p^x + \omega^{tx}p^z - \omega^{xz}p^t), \quad (3.34)$$

$$P^z(p) = -\frac{1}{8m \int d\Sigma_\lambda p^\lambda n_F} \int d\Sigma_\lambda p^\lambda 2n_F(1 - n_F)(-\omega^{ty}p^x + \omega^{tx}p^y - \omega^{xy}p^t). \quad (3.35)$$

For particles with spin bigger than  $1/2$ , the definition of the polarization requires the introduction of another quantity, the full-spin density matrix  $\Theta_{ij}$ . For example, for particles with spin 1, this matrix is used in the definition of an observable called alignment, responsible for the orientation of spin of the ensemble being studied [25]. Since this discussion is out of the scope of this work, we focus on the polarization of spin- $1/2$  particles.

### 3.5 The $\mathcal{R}$ Observable

As we show on Fig. 3.4, the effect of a jet passing through the QGP is that of forming a “smoke ring” structure, with a vorticity distribution in the plane perpendicular to the direction of the jet. In this context, an observable  $\overline{\mathcal{R}}_\Lambda^{\hat{t}}$  was proposed by Lisa et. al. [72] as a measurable quantity of the vorticity (and consequently the polarization) formed in the ring. This observable, written in terms of the polarization vector  $\vec{P}$  defined in Eqs. (3.33-3.35), has the form

$$\overline{\mathcal{R}}_\Lambda^{\hat{t}} \equiv \left\langle \frac{\vec{P}_\Lambda \cdot (\hat{t} \times \vec{p}_\Lambda)}{|\hat{t} \times \vec{p}_\Lambda|} \right\rangle_{p_{T,y}}, \quad (3.36)$$

where  $\hat{t}$  is the trigger direction of the smoke ring, and  $\langle \cdot \rangle$  is the weighted average over the transverse momentum and the rapidity, using the  $\Lambda$  multiplicity as weight.

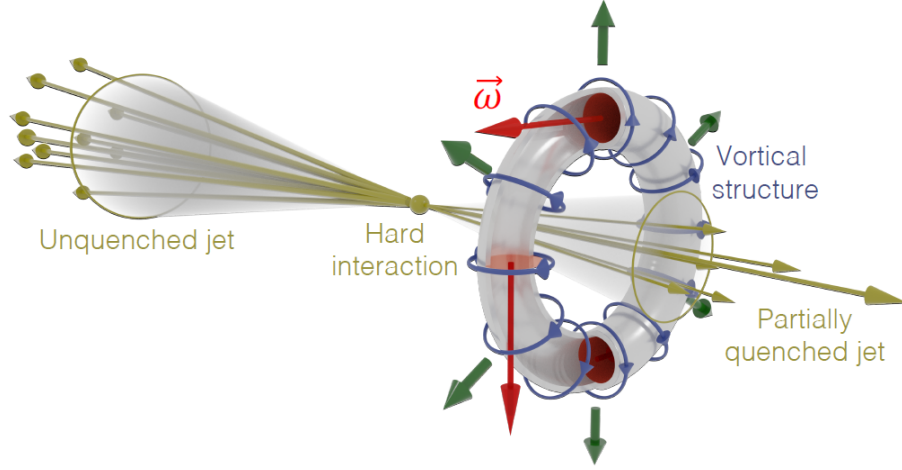


Figure 3.4: Illustration of the physical situation in which a dijet is created inside the QGP. One component is quenched by the medium, forming a vortical structure, while the other is proceeds unquenched [26].

The importance of the ring observable comes into play when we are interested in analysing the effects of the polarization generated by the vorticity ring only. Let's suppose, for example, that a jet travels in the positive  $x$  direction, forming a vorticity ring in the  $yz$  plane. If we want to compute the magnitude of the polarization, the information of the polarization in the transverse plane will average to zero and we will lose the contributions of  $\vec{P}_\Lambda$  in this direction, since the transverse components are antisymmetric. To better visualize this scenario, we show on Fig. 3.5 the vectors involved in the analysis of the  $\overline{\mathcal{R}}_\Lambda^{\hat{t}}$  observable. The cross product between the direction of the jet  $\hat{t}$  and the momentum of the  $\Lambda$  particle will be in the same direction as the vorticity vector  $\omega^\mu$ , defined in Eq. (3.29). As such, the dot product in the numerator of Eq. (3.36) will maximize the values of  $\vec{P}_\Lambda$  in the transverse plane, yielding a more straightforward analysis of the ring.

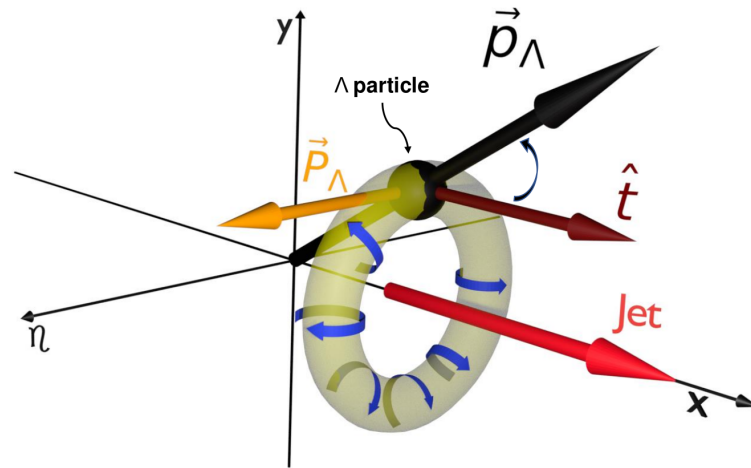


Figure 3.5: Illustration of the vectors involved in the analysis of the  $\mathcal{R}$  observable. The dot product between the vector  $\vec{P}_\Lambda$  and  $(\hat{t} \times \vec{p}_\Lambda)$  will maximize the polarization values in the direction of the vorticity ring, making  $\overline{\mathcal{R}}_\Lambda^{\hat{t}}$  a suited observable to describe the polarization effects in the transverse plane of the jet.

# Methodology

In this chapter, we present the methodology for the simulations used in this work. The steps we simulate in our model can be divided in three parts: creation of initial conditions (ICs), evolution of the initial conditions in a (3+1)D relativistic hydrodynamic framework and analysis of the  $\Lambda$  particles. In the next sections, we will introduce the details for the simulation of the jet thermalization passing through the QGP. In our case, we don't simulate the jet per se, but rather the energy it deposits on the fluid. To achieve that we use an energy-momentum tensor to compute the jet parameters that will later be used by the IC and the hydrodynamic code.

## • Initial Condition

The initial conditions are responsible for generating energy profiles that will be used by the hydrodynamic simulations to compute the dynamics of the fluid. In our simulation chain, initial conditions are generated by a code known as T<sub>R</sub>ENTo 3D [73], a model that considers a nucleon distribution from a colliding nucleus using optical potentials, and computes the energy deposited considering a Glauber geometrical model to simulate the inelastic cross-section and the collisions between the nuclei. This energy deposition is translated into the components of the energy-momentum tensor  $T^{\mu\nu}$ , which is used by hydrodynamic code to solve the conservation equation  $\partial_\mu T^{\mu\nu} = 0$  to calculate the dynamical evolution of the system.

In order to simplify the problem of generating an initial condition, we studied the case where the background has no fluctuations of energy. We simulate a smooth initial condition by averaging over a thousand T<sub>R</sub>ENTo 3D simulations, configured to Pb-Pb collisions with center of mass energy  $\sqrt{s_{NN}} = 2.76$  TeV and impact parameter  $b = 0$  fm. Figure 4.1 shows the results of this procedure. On the top row, on Fig. 4.1a, we

show an example of the energy density profile generated by T<sub>R</sub>ENTo for a single event, projected on the  $xy$  plane for  $\eta = 0$ . On Fig. 4.1b we show the 3D surface view of the same profile. We note that for single events, the energy distribution tends to be non-uniform, with high and low areas representing the fluctuations of each binary collision between nucleons of the nucleus. On Figs. 4.1c and 4.1d we show the result of our procedure to generate a smooth initial condition, where the energy deposition was averaged over a thousand events. In this case, we have a Gaussian-like distribution on the three spacial direction. This will be our choice for simulating the fluid expansion. The grid in which the energy density is distributed is an  $(x, y, \eta_s)$  grid, with spacing  $dx = 0.1$  fm,  $dy = 0.1$  fm and  $d\eta_s = 0.2$ . More about the specific parameters used in T<sub>R</sub>ENTo 3D can be found in Refs. [26, 29, 73].

The jet thermalization is modeled based on a dijet formation in the Quark-Gluon Plasma. In our calculations [26], we use data from the ATLAS Detector at the LHC to compute an approximate value for the energy and momentum of the thermalized jet. The jet asymmetry observables  $A_J$  and  $x_J$ , defined as

$$x_J \equiv p_{T_2}/p_{T_1}, \quad (4.1)$$

$$A_J \equiv (E_{T_1} - E_{T_2})/(E_{T_1} + E_{T_2}), \quad (4.2)$$

where the index “1” and “2” denotes respectively the unquenched and quenched jet components, are used to obtain the energy  $E_{th} = E_{T_1} - E_{T_2}$  and momentum  $p_{th} = p_{T_1} - p_{T_2}$  of the thermalized jet. From the distribution of  $dN/dA_j$  and  $dN/x_J$  for a central Pb–Pb collisions at  $\sqrt{s_{NN}} = 2.76$  TeV [74, 75], we choose the values of  $A_J$  and  $x_J$  with higher multiplicity, yielding  $A_J = 0.425$  and  $x_J = 0.525$ . Also from Refs. [74, 75], we obtain the values of  $p_{T_1} = 89.5$  GeV and  $E_{T_1} = 100$  GeV for the unquenched jet and compute the energy  $E_{th} = 59.5$  GeV and the momentum  $p_{th} = 43$  GeV of the thermalized jet. With these quantities, we modify our averaged initial condition to contain a spherical region of higher energy density, centered at the origin with radius  $x = 0.5$  fm,  $y = 0.5$  fm and  $z \approx 0.3$  fm. In the Milne coordinates - Eqs. (2.20) and (2.21) - the spacial rapidity and proper time are  $\eta_s \approx 1.0$  and  $\tau = 0.25$  fm/c.

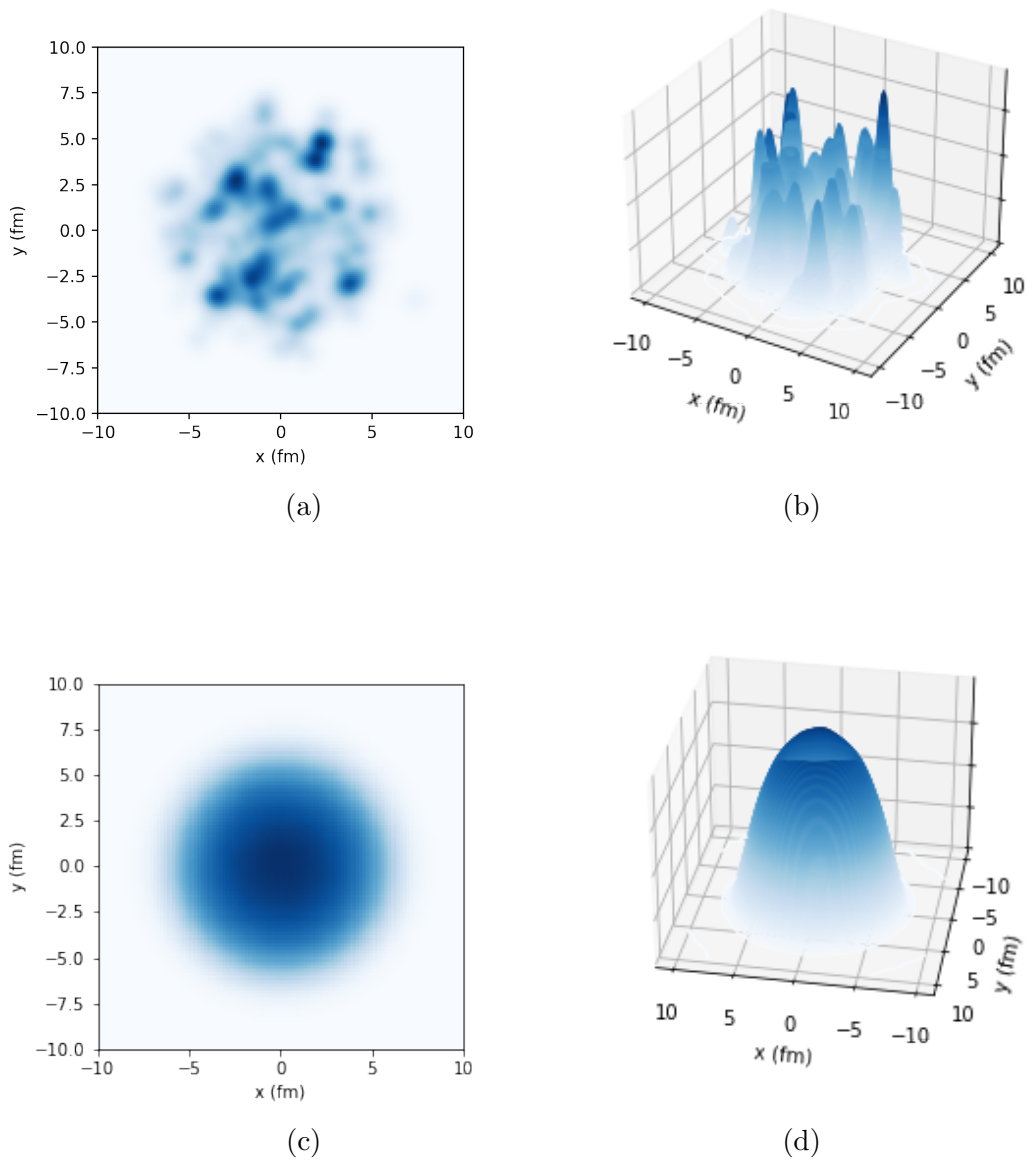


Figure 4.1: Energy density profiles from T<sub>RENT</sub>O simulations for two scenarios of initial conditions. (a) shows the energy distribution for a single event as a function of  $x$  and  $y$ , projected for  $\eta_s = 0$ , and (b) its surface view. We note the formation of non-uniform structures. (c) and (d) shows a similar scenario, but for a smooth initial condition, averaged over a thousand events.

### • The Jet Thermalization Model

The methodology we use to estimate the energy density and velocity values of the jet thermalization consists in solving the eigenvalue problem  $T^{\mu\nu}u_\nu = \epsilon u^\mu$ , in a procedure called Landau matching. In our model, we build an energy-momentum tensor in terms of the thermalized four-momentum  $p_{th}$ , thermalized energy  $E_{th}$  and the system volume  $V$ ,

$$T^{\mu\nu} = \frac{1}{V} \frac{p_{th}^\mu p_{th}^\nu}{E_{th}}. \quad (4.3)$$

Using the fact that our jet is traveling in the  $+x$  direction, the four-momentum and four-velocity will have only the time and  $x$  components,

$$p_{th}^\mu = (E_{th}, p_{th}, 0, 0), \quad (4.4)$$

$$u_\mu = (u_\tau, u_x, 0, 0). \quad (4.5)$$

Thus, the Landau matching equation can be solved for  $\epsilon$  and  $u_\mu$  using the energy-momentum tensor from Eq. (4.3), yielding

$$\epsilon = \frac{1}{V} \frac{E_{th}^2 - p_{th}^2}{E_{th}}, \quad (4.6)$$

$$u_x = \frac{p_{th}}{\sqrt{E_{th}^2 - p_{th}^2}}. \quad (4.7)$$

Inserting the values of  $E_{th}$  and  $p_{th}$  in the previous equations, and writing the boosted velocity as  $u_x = \gamma v_x$ , we find the total energy and the speed in the  $+x$  direction to be  $\epsilon V = 30$  GeV and  $v_x = 0.7c$ . These are the main quantities used to build our jet thermalization model. This procedure was also used by Ref. [76] to calculate the  $\Lambda$  global polarization in heavy-ion collisions.

In our simulations, the first step of the hydrodynamic evolution of the QGP happens at  $\tau = 0.25$  fm/c. At this time, the code responsible to run the fluid dynamics receives the initial condition. For each step of  $\Delta\tau = 0.05$  fm/c, it solves the relativistic hydrodynamic equations, describing the fluid state at the given time. The outputs are the evolution parameters, such as the local energy density and viscosity of the fluid. When the proper time  $\tau$  reaches somewhere between 10 fm/c and 12 fm/c, all medium will have

already passed the freeze-out temperature of 151 MeV, and the evolution will stop. Our (3+1)D hydrodynamic code is configured to output the important parameters, such as energy density and vorticity, in the form of 3D histograms. These objects are built in a way that the usual coordinates system is the  $(x, y, \eta_s)$ , with the bin contents being the desired quantity to be studied. The grid in which the hydro code evolves the initial condition has 281 steps, going from  $-14$  fm to  $14$  fm in both  $x$  and  $y$  directions, and 201 steps, going from  $-10$  fm to  $10$  fm in the  $\eta_s$  direction. The size of the grid used in the calculation is such that the entire evolution of the system is within this volume.

The energy density of the initial condition for a plain background (without any jet thermalization) can be seen in Fig. 4.2. The top Fig. is obtained by taking a slice of the energy density histogram at  $\eta_s = 0$ . The colormap indicates the intensity of the energy density, showing a maximum of  $200 \text{ GeV}/\text{fm}^3$  around the origin. The bottom Fig. is a projection of the top Fig. in the  $x$  axis for different  $\tau$  values. It shows that the initial condition behaves like a Gaussian distribution, extending from  $-10$  fm to  $10$  fm ( $y$  and  $\eta_s$  directions also have a similar Gaussian distribution). As the proper time evolves, we see that the energy density of the medium dissipates throughout the grid. As this dissipation happens, a fluid located at the central area of the grid, for example, moves towards the edges and eventually reaches  $T = 151$  MeV. With that in mind, we've built a grid big enough so that everything that goes out of the box always have a temperature lower than the freeze-out temperature. Hence, for  $\tau = 0.25 \text{ fm}/c$ ,  $\tau = 1.25 \text{ fm}/c$  and  $\tau = 10 \text{ fm}/c$ , the energy density of the Gaussian peak decreases from  $200 \text{ GeV}/\text{fm}^3$  to  $30 \text{ GeV}/\text{fm}^3$  and  $1 \text{ GeV}/\text{fm}^3$ , respectively.

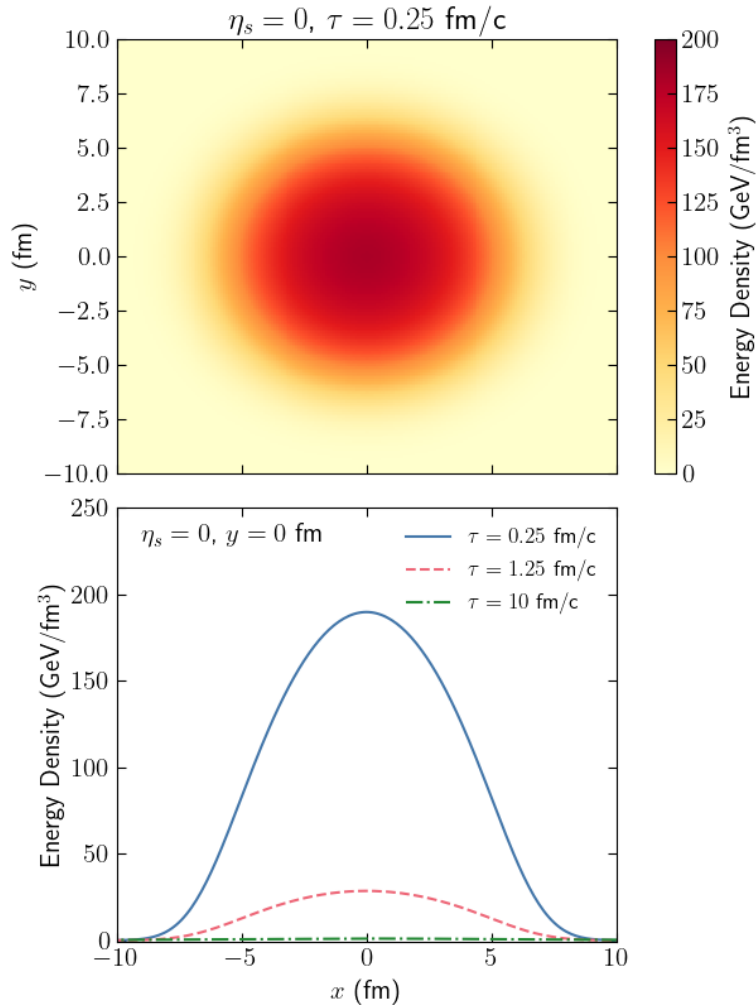


Figure 4.2: Initial condition of the energy density without the jet thermalization. The top plot shows the energy density as a function of the positions  $x$  and  $y$ , for  $\eta_s = 0$ . The bottom plot shows the energy density profile as a function of  $x$ , for  $y = 0 \text{ fm}$  and  $\eta_s = 0$ , for three different times of evolution,  $\tau = 0.25 \text{ fm/c}$ ,  $\tau = 1.25 \text{ fm/c}$  and  $\tau = 10 \text{ fm/c}$ . We note that the energy decreases as the proper time evolves.

Once created the energy density background in the evolution, we add a sphere of fixed  $\epsilon$  on top of the Gaussian profile, centered at the origin and with a velocity pointing in the  $+x$  direction. This sphere, with size of 0.5 fm in the  $x$  and  $y$  directions, and  $\approx 1.0$  in the  $\eta_s$  direction, represents the energy deposited by the jet in the fluid. Figure 4.3 shows the 2D and 1D profiles of the thermalized energy on top of the background, for  $\tau = 0.25 \text{ fm/c}$ . From the upper plot we see that the thermalization is a high energy density sphere centered at the origin, with a total value of  $300 \text{ GeV}/\text{fm}^3$ . The lower plot depicts its  $x$  profile, showing that that jet thermalization alone has around  $100 \text{ GeV}/\text{fm}^3$  of energy density above the background.

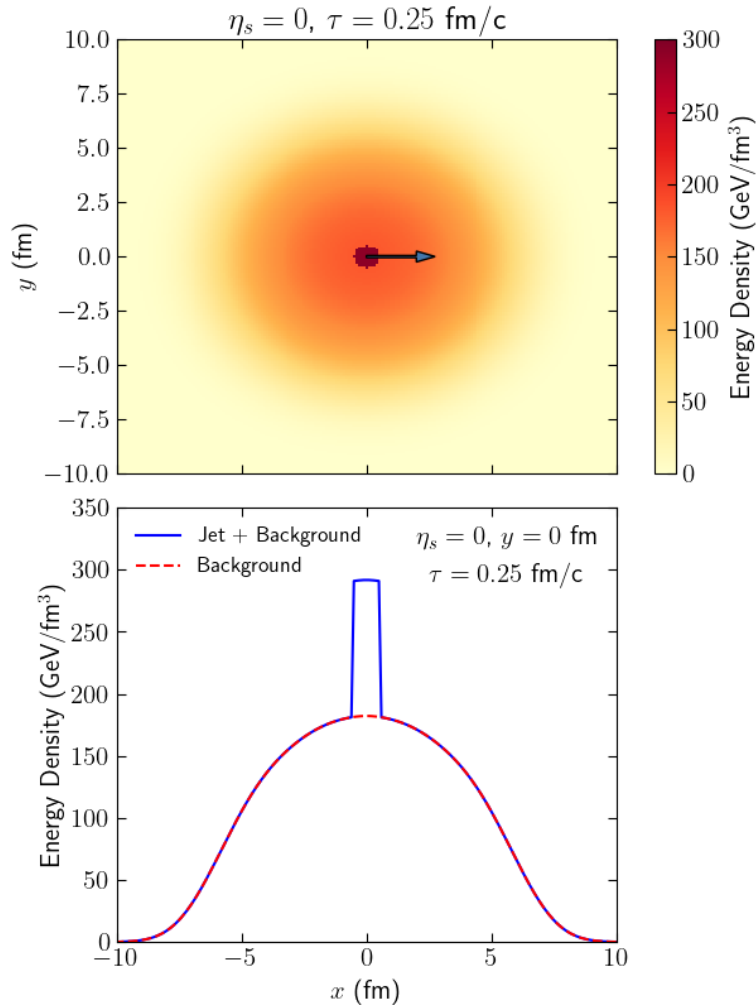


Figure 4.3: Initial condition of the thermalization on top of the background fluid. The top plot shows the energy density as a function of the positions  $x$  and  $y$ , for  $\eta_s = 0$ . We note the jet thermalization as the high-density region centered at  $(x, y, \eta_s) = (0, 0, 0)$ . The bottom plot shows the projection of the initial energy density (red curve) with the jet thermalization (blue curve), for  $y = 0$  fm and  $\eta_s = 0$ .

### • Hydrodynamic Simulations and Particlization

The hydrodynamics code is responsible for taking our initial condition, generated by T<sub>R</sub>ENTo 3D, and simulating the expansion of the Quark-Gluon Plasma. In this step, we use a (3+1)D relativistic hydrodynamics code [28] that can be set up to run in both ideal and viscous cases. The model solves numerically the conservation equation  $\partial_\mu T^{\mu\nu} = 0$  for each cell in the grid. For completeness, we write again the ideal and viscous expressions for the tensor,

$$T_{ideal}^{\mu\nu} = \epsilon u^\mu u^\nu - P(g^{\mu\nu} - u^\mu u^\nu), \quad (4.8)$$

$$T_{visc}^{\mu\nu} = \epsilon u^\mu u^\nu - (P + \Pi)(g^{\mu\nu} - u^\mu u^\nu) + \pi^{\mu\nu}, \quad (4.9)$$

where  $P$  is the pressure,  $\Pi$  is the bulk pressure and  $\pi^{\mu\nu}$  is the shear viscosity tensor. In the ideal scenario, the solution of the hydrodynamics equation is complemented by an equation of state that relates the pressure  $P$  to the energy density  $\epsilon$ . This relationship is based on the assumption of local thermal equilibrium, that allows the use thermodynamic equations to obtain local properties of the fluid, such as energy density, pressure and temperature. Therefore, with a relation such as  $P = P(\epsilon)$ , a closed set of differential equations is solved by the hydrodynamic code. The viscous scenario, on the other hand, needs not only the conservation equation and equation of state, but also the equations of motion for the bulk pressure and shear tensor [77, 78]. For the simulations done in this work, we vary the temperature independent viscosity values and use the Lattice-QCD based equation of state, from the HotQCD collaboration [79].

Finally, the hydrodynamic description of the plasma comes to an end as the fluid reaches the free-streaming temperature of  $T_{FS} = 151$  MeV. At this point, all the medium that was being described by relativistic fluid dynamics is converted into free-streaming particles. This process is called particlization, and the surface that connects all the points  $(\tau, x, y, \eta_s)$  at which the temperature of the fluid has achieved a value below  $T_{FS}$  is called particlization hypersurface. The final code, iSpectraSampler (iSS) [80], describes the particles created on the hypersurface based on the Cooper-Frye algorithm [81]. The iSS uses the probability of a particle being emitted from a freeze-out cell with a specified momentum to generate a description of momentum and position of the final particles of the collision. With this information, we modified the code so that iSS automatically computes the polarization of  $\Lambda$ 's based on their momentum and on the thermal vorticity of the fluid cell it was created. We discussed more about the polarization and thermal vorticity in Chapter 3.

# Results

In this chapter we show results of our simulations regarding the model of jet thermalization in the Quark-Gluon Plasma, and its implications on the polarization of  $\Lambda$  particles. We begin with a systematic study, analysing both energy density and vorticity throughout different times of the hydrodynamics evolution. Also, we analyse the polarization of the  $\Lambda$  particles and compute the correspondingly ring observable  $\overline{\mathcal{R}}_{\Lambda}^{\hat{t}}$ . These final observables will give us a measure of how strong is the coupling between the vorticity and the spin of the  $\Lambda$ 's.

## 5.1 Systematic Study of the Jet Thermalization

As soon as the hydrodynamic simulation receives the initial condition, it starts solving the dynamics equation of the fluid and builds up the evolution pattern of our model. In Fig. 5.1 we show the thermalized jet evolution at  $\tau = 1.25$  fm/c, after  $\Delta\tau = 1.00$  fm/c have passed from the initial condition. Compared to the initial condition in Fig. 4.3, the peak energy density at time  $\tau = 1.25$  fm/c decreased from  $300$  GeV/fm<sup>3</sup> to  $80$  GeV/fm<sup>3</sup>. Since the background also decreases, if we analyse only the reduction of the hot spot created by the jet thermalization, we see a decrease of  $\sim 100$  GeV/fm<sup>3</sup> to approximately  $50$  GeV/fm<sup>3</sup>. This decrease in the jet energy reflect the dissipation effects it deposits on the medium.

The fact that the jet moves to the right introduces a region of lower energy in its path. This effect is shown in the bottom plot of Fig. 5.1, where the  $x$  projection of the energy density is plotted. The peak at  $x = 1$  fm leaves behind a small depression that drops below the background curve. This happens because the high momentum of

the jet induces the background to move along with it, creating this energy density gap on its way.

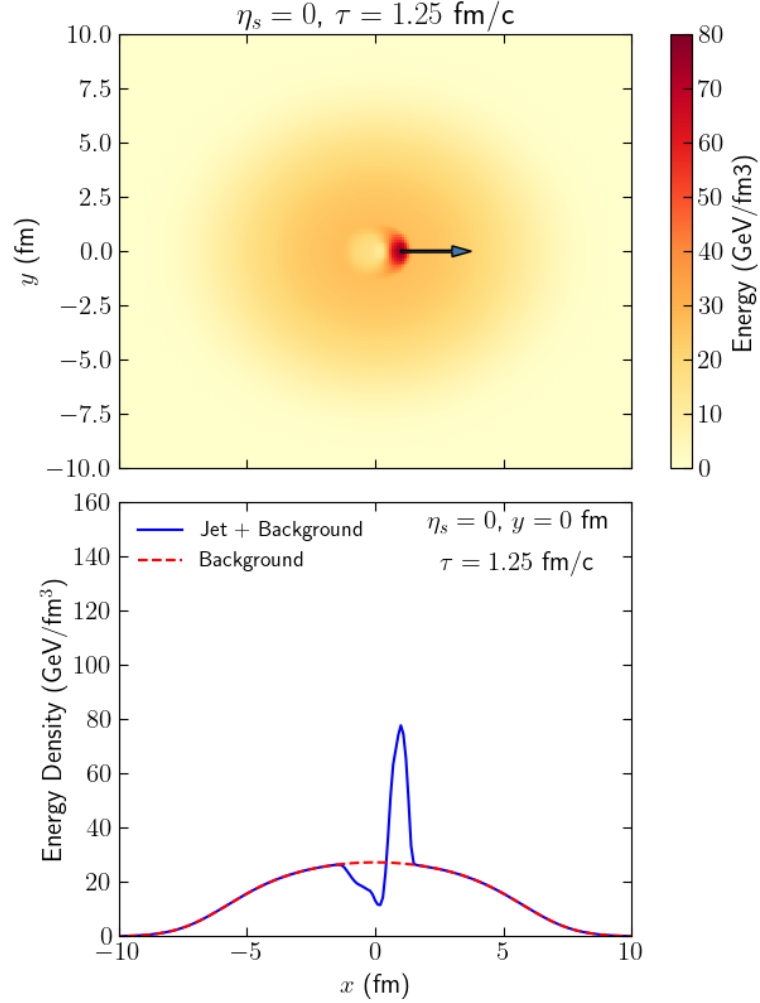


Figure 5.1: Evolution of the thermalized jet after  $\Delta\tau = 1.00$  fm/c of the initial condition. The top plot shows a colormap of the energy density as a function of the positions  $y$  and  $x$ , for a slice in  $\eta_s = 0$  and  $\tau = 1.25$  fm/c. The bottom plot shows the projection of the energy density in the  $\eta_s = 0$  and  $y = 0$  fm directions, for  $\tau = 1.25$  fm/c. The blue curve represents the jet thermalization with the background fluid, while the red curve represents background fluid simulated without the jet. We note that the high momentum of the jet thermalization induces a gap region on the background fluid. This can also be seen on the top plot as high-yellow circle centered at  $x = 0$  fm and  $y = 0$  fm.

As the system evolves in time, the expansion causes the energy density of every point in space to reduce. The dynamics of the energy density evolution in each point will thus depend on the expansion of the system and also on the propagation of the inserted initial jet energy through the medium. Figure 5.2 shows the energy density evolution versus tau for two specific points of the hydrodynamical grid calculation. As  $\tau$  increases, there is a decrease of the energy density at these two fixed points due to the general

expansion of the fluid. The blue curve, for instance, has a sudden drop at the initial times, representing the gap formation due to the jet movement at  $(0, 0, 0)$ . Likewise, the red curve, representing the energy density at the point  $(5, 0, 0)$ , has a constant drop of energy up to  $\tau \approx 6$  fm/c, where the small bump indicates that the jet has passed on that point.

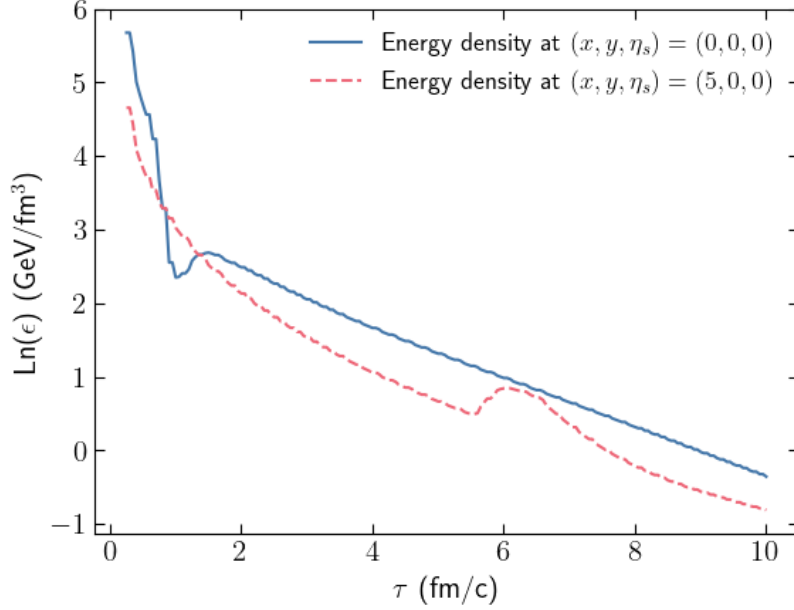


Figure 5.2: Comparison of the natural log of the energy density as a function of  $\tau$  for two points of the grid,  $(x, y, \eta_s) = (0, 0, 0)$  and  $(x, y, \eta_s) = (5, 0, 0)$ . We note that the jet thermalization passes through  $(5, 0, 0)$  around  $\tau = 6$  fm/c, represented by the bump in the red curve, and introduces a vacuum region at  $(0, 0, 0)$ , represented by the fast drop of the blue curve at the beginning of the evolution.

As the thermalized jet travels through the fluid, it deposits part of its energy in the medium. The drop in the internal energy of the jet thermalization, also known as thermal energy, can be seen in Fig. 5.3, where we display the energy integrated over  $x$ ,  $y$  and  $\eta_s$  axis as a function of  $\tau$ , for three different viscosities. We note that in the ideal case the jet loses energy slower to the medium, while in the viscous case both red and green curves drop faster. The fast energy increase in the initial times are related to the high pressure gradients the thermalized jet is subjected to. As we put an extremely high energy density region in a initially uniform fluid, this thermalized region will be uniformly compressed and its internal energy will increase.

One important element in the evolution of the jet is the dynamics encoded in the relativistic velocity  $u_x$ . The velocity of the thermalized jet versus  $\tau$  is seen on Fig. 5.4.

We note that the effects of the fast expansion of the jet and the high pressure gradients it imposes to the medium are translated into the increase of  $u_x$  at the beginning of the evolution. This is followed by the decrease of the velocity due to the dissipation of the jet kinetic energy to the fluid - for higher viscosities, the jet loses more velocity to the medium.

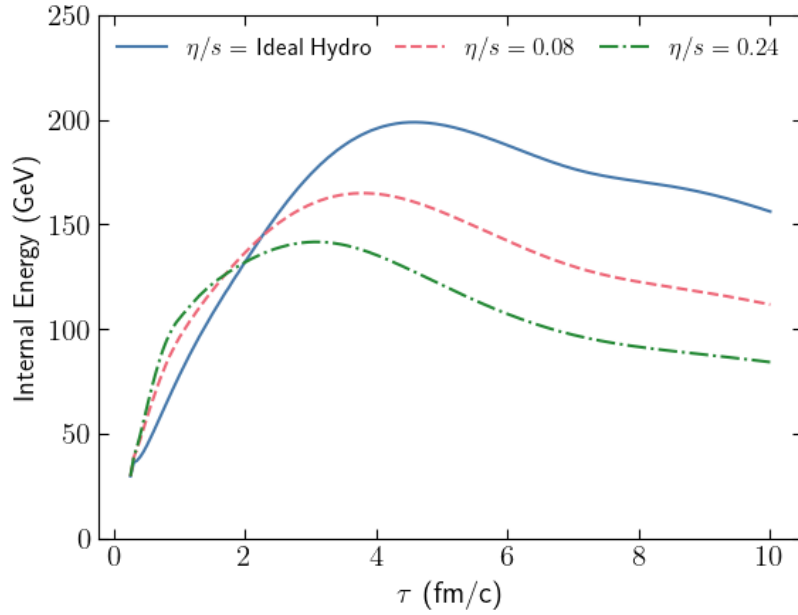


Figure 5.3: Internal energy of the thermalized jet integrated over  $x$ ,  $y$  and  $\eta_s$  as a function of  $\tau$ . We observe the differences in the energy drop for different values of viscosity. The increase of internal energy is caused by the high pressure gradients the medium imposes to the thermalized jet.

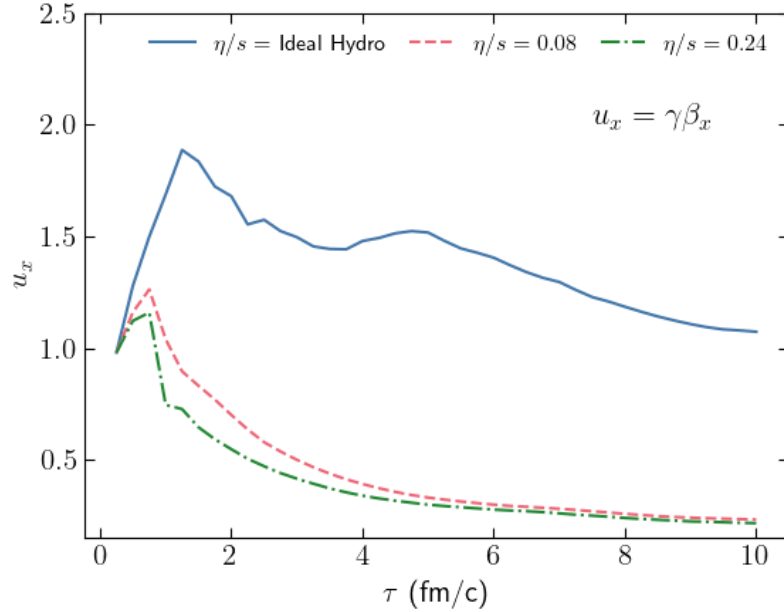


Figure 5.4: Velocity of the jet thermalization as a function of  $\tau$ . We note that the velocity is dissipated faster for higher viscosities, while the initial increase of  $u_x$  reflects the fast expansion and high pressure gradients the thermalized jet imposes to the medium.

We've analysed so far hydrodynamic simulations with specific viscosity values of 0.0, 0.08 and 0.24. As this viscosity changes, we see a change in the behaviour of the jet as well - the bigger the specific viscosity is, the more energy the jet dissipates in the medium. In Fig. 5.5 we show the evolution of the relative maximum value of the jet energy density plotted for different values of viscosity. In this plot, all curves were scaled by the values obtained from the simulation considering ideal hydrodynamics. From the plot, we note that as  $\eta/s$  increases, the thermalized jet loses more energy to the bulk fluid. The region between  $0.25 \text{ fm}/c < \tau < 1 \text{ fm}/c$  is the gap response to the energy deposited, indicating that a more viscous medium makes the jet displace more fluid at the beginning of the evolution.

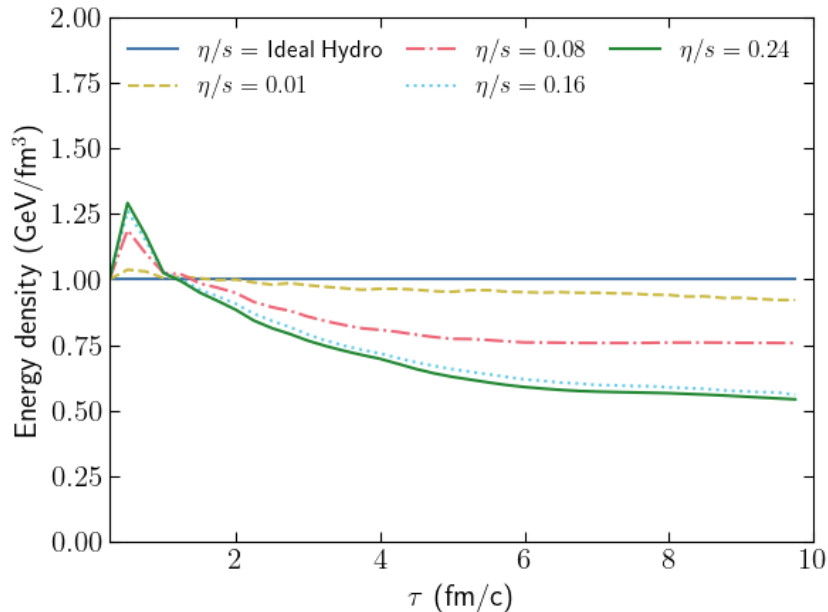


Figure 5.5: Comparison of the maximum value of energy density of the jet as a function of the time  $\tau$ , for different viscosity values. All curves have been scaled by the results obtained from the ideal hydrodynamics case. We note that the energy density drops faster for higher values of viscosity.

Until now we’ve been interested in studying the energy density of the jet thermalization inside the QGP, as well as the medium response to its movement. But the motion of the jet in this relativistic fluid also creates velocity gradients that tends to swirl around jet, introducing angular momentum, and consequently vorticity, to the system. Let’s now turn our attention to the vortical structures formed due to the jet thermalization inside the Quark-Gluon Plasma.

We expect, intuitively, that the effect of a jet passing through a relativistic fluid is similar to that of a projectile passing through a bucket of water, or even a puff of smoke forming a “smoke ring” on the air. Indeed, in our simulation, this vortical pattern is seen in the direction perpendicular to the jet axis. Figure 5.6 shows the vorticity ring in the  $(y, \eta_s)$  plane, sliced at  $x = 0.3$  fm and at time  $\tau = 2.25$  fm. The colormap represents the value of  $|\vec{w}| = \sqrt{(w^x)^2 + (w^y)^2 + (w^z)^2}$ , while the black arrows indicates the directions of the  $y$  and  $z$  components of the thermal vorticity, defined in Eq. (3.29).

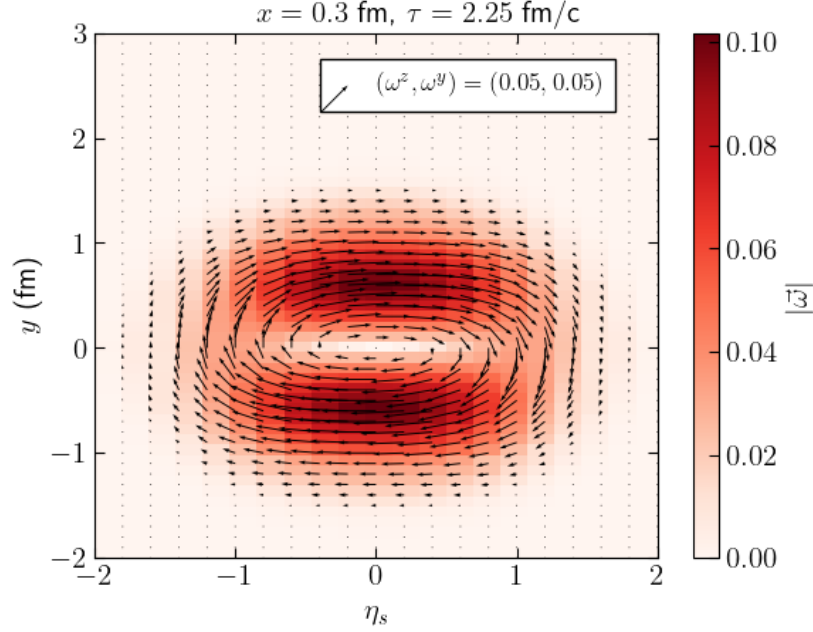


Figure 5.6: Vorticity ring generated by the thermalization of the jet in the fluid. The ring is shown in the  $(y, \eta_s)$  plane, after  $\Delta\tau = 2$  fm/c of the hydrodynamic evolution. The colormap represents the absolute value of the vorticity vector, plotted as a function of the positions  $y$  and  $\eta_s$ , for a slice in  $x = 4$  fm. The arrows show how the components  $\omega^z$  and  $\omega^y$  generate the vorticity gradient of the ring.

As the thermalized jet moves inside the QGP, it deposits momentum in the  $x$  direction and creates a velocity gradient on its way. In Fig. 5.7 we show a projection of the  $z$  component of the vorticity in the  $(x, y)$  plane, for a slice of  $\eta_s = 0$ . The yellow dot represents the position of the jet, where the energy density is maximum, and the black arrows are the  $x$  and  $y$  components of the four-velocity. We see that the velocity field has a more accentuated curl close to the maximum values of vorticity: for  $w_z > 0$  (red area) the arrows curve counter-clockwise, while for  $w_z < 0$  (blue area) the arrows curve clockwise.

Similar to the classical hydrodynamics, the dynamics of the Quark-Gluon Plasma also experiences resistance to the movement in the form of shear ( $\eta$ ) and bulk ( $\xi$ ) viscosity. While the first one is related to the fluid's resistance to friction and loss of kinetic energy to the system, the second is related to the fluid's bulk expansion. In our simulations, we tested the effect of turning on the bulk viscosity, while maintaining the specific shear viscosity value of  $\eta/s = 0.08$ . The result is shown in Fig. 5.8, where only the positive component of  $\omega_z$  was considered ( $0 \text{ fm} < y < 8 \text{ fm}$ ). At the beginning of the simulation we note a fast increase of  $\omega_z$  due to our initial condition causing a sudden

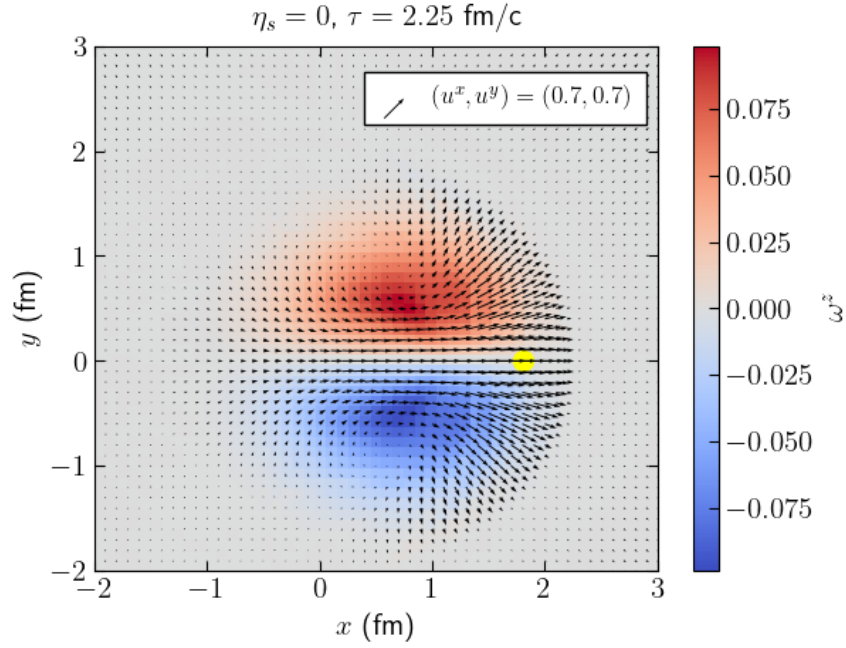


Figure 5.7: Component  $\omega^z$  of the vorticity as a function of the positions  $x$  and  $y$ , for a slice in  $\eta_s = 0$  and time  $\tau = 2.25$  fm/c. The arrows are formed by the components  $x$  and  $y$  of the four-velocity, with an accentuated curl close to the region of maximum vorticity. The yellow dot represents the position of the thermalized jet in the simulation.

disturbance in the background fluid - we create a high energy density area with a high velocity in a relative slow moving fluid. After this initial interval, the simulation is able to evolve normally. We note that the bulk viscosity interferes very little with the  $z$  component of the thermal vorticity. With this behavior in mind, we can finally compare the effects of varying only the shear viscosity values in our observable  $\omega_z$ , without considering the effects of the bulk viscosity. In Fig. 5.9 we show this comparison for the positive region of  $\omega_z$ . We observe that for higher viscosity values, the vorticity generated by the thermalized jet is smaller, but the reduction of the vorticity with time seems to follow the same trend.

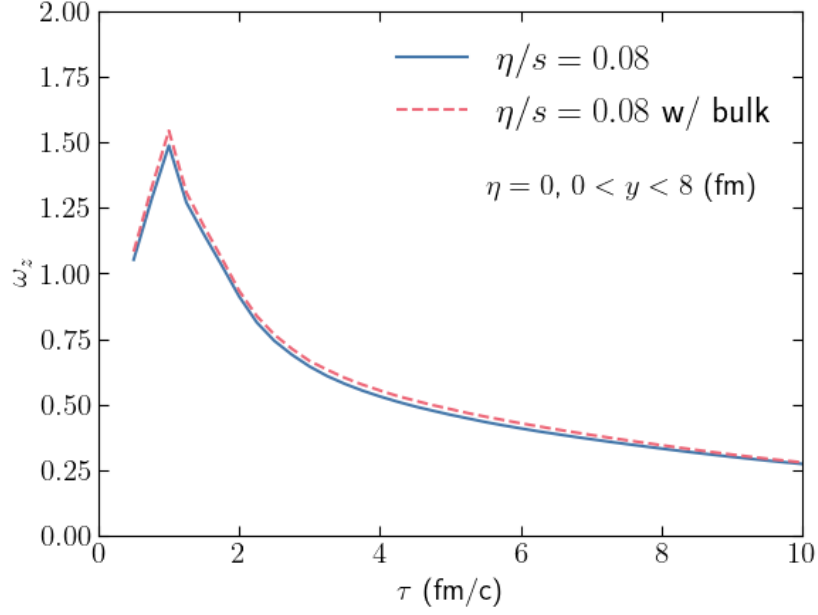


Figure 5.8: Component  $z$  of the thermal vorticity versus the time  $\tau$  for two different simulations: one considering the shear plus bulk viscosities (red curve), and one considering only the shear viscosity (blue curve). We note that the bulk viscosity has a slight change in the behavior of  $\omega_z$ .

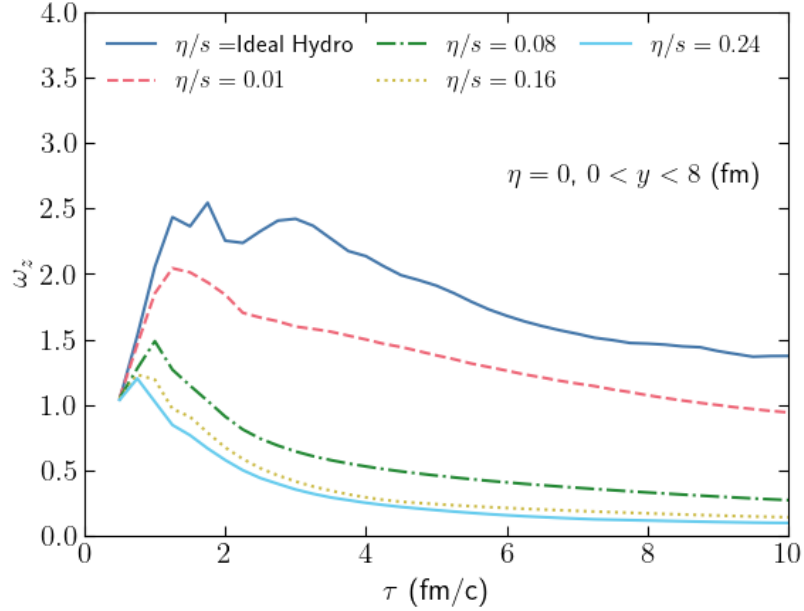


Figure 5.9: Maximum value of the positive part of the component  $\omega_z$  as a function of the proper time  $\tau$ , sliced at  $\eta_s = 0$  and  $0 < y < 8$  fm. We note that the vorticity induced by the jet is lower for cases where the medium shear viscosity is higher, but the shape of the reduction curve in time seems to be the same.

## 5.2 Final Observables

After studying the energy density and vorticity observables of the thermalized jet evolution in the QGP, we turn our attention to the final observables related to the polarization of the  $\Lambda$  particles. As we mentioned in Chapter 3, the vorticity generated on the hydrodynamic cells will induce a polarization of the fermions created at the particlization hypersurface. In this context, the  $\Lambda$  hyperon is an ideal candidate to be analysed, since we are able to determine its spin directly from its decay topology. In this section we begin our analysis of the final observables by verifying the relation between the vorticity  $\omega_z$  computed on the particlization hypersurface and the  $\Lambda$  polarization. Figure 5.10 shows this correlation, linking the average value of the  $z$  component of the vorticity, calculated from the particlization hypersurface in the range  $|\eta_s| < 0.5$ , to the  $\Lambda$  polarization  $P_z$ , at  $|y| < 0.5$  and  $p_T < 3.0$  GeV/ $c$ . The pseudorapidity range considered here corresponds to the mid rapidity region that is accessible to most collider experiments like ALICE at the LHC and STAR at RHIC. Also, since we put the thermalized jet at  $y = 0$  and  $\phi = 0$ , it is reasonable to only analyse this interval. The  $p_T$  range is the region considered to be in the validity range of hydrodynamical simulations. In Fig. 5.10, the x axis is the azimuthal angle, computed for the vorticity curve using the four-velocity components,  $\varphi = \arctan(u^y/u^x)$ , and for the polarization curve using the four-momentum components,  $\varphi = \arctan(p^y/p^x)$ . The agreement in positions of maximum and minimum of the two curves is shown in Fig. 5.10. The vorticity and the polarization indicate a clear correlation between these two parameters, which shows that indeed the net vorticity of the hydro-fluid cells will yield a net polarization of the Lambdas. At first, this might look like a trivial observation, but it was not clear that the statistical nature of particlization process would not eliminate this correlation. Hence, the observation of the correlations between the two curves is a strong indication that indeed the Lambda polarization is a good candidate to observe experimentally the formation of vortices in the Quark-Gluon Plasma.

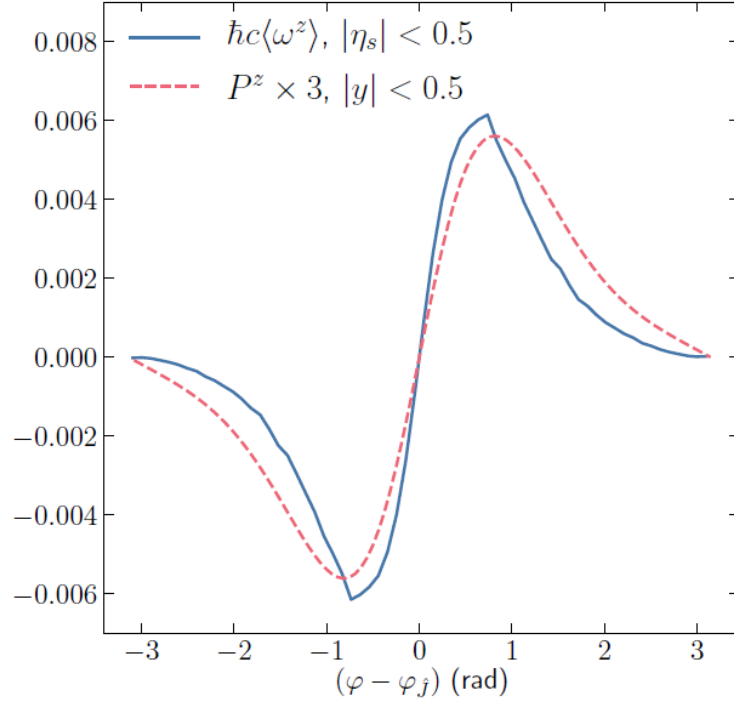


Figure 5.10: Correlation between the averaged  $z$  component of the vorticity at the particleization hypersurface and the weighted-average of the  $z$  component of the polarization of the  $\Lambda$  particles. The  $y$  axis represents the magnitude of each component as a function of the azimuthal angle, calculated as  $\phi = \arctan(u^y/u^x)$  for the vorticity and  $\phi = \arctan(p^y/p^x)$  for the polarization.

In Fig. 5.11 we show the dependence of the Lambda polarization in the  $z$  direction,  $P_z$ , as a function of the relative angle  $(\varphi - \varphi_j)$  and the transverse momentum of the  $\Lambda$ . The dotted marks indicates the position where  $|P_z|$  has the maximum value for each bin of  $p_T$ . We note that for high values momentum, the dots are closer to  $\varphi - \varphi_j = 0$ , indicating that the maximum values of  $|P_z|$  are closer to the jet axis. Also, the  $z$  component of the polarization is higher for particles within the momentum range  $0.5 \text{ GeV}/c < p_T < 1.0 \text{ GeV}/c$ .

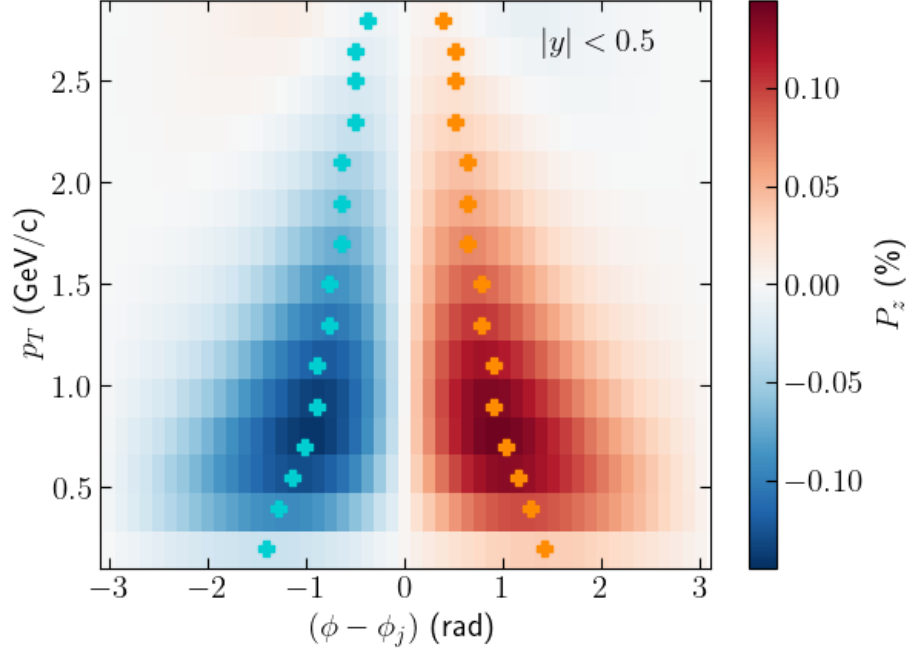


Figure 5.11: Distribution of the weighted average of the component  $P_z$  of the Lambda polarization, as a function of the momentum  $p_T$  and the azimuthal angle relative to the jet direction. The colored dots represent the bins of  $p_T$  where  $|P_z|$  has a maximum value.

Now, we turn our attention to the ring observable  $\overline{\mathcal{R}}_\Lambda^t$ , defined in Eq. (3.36). We compute the value of  $\overline{\mathcal{R}}_\Lambda^t$  for each value of momentum in the range  $0.5 \text{ GeV}/c < p_T < 3.0 \text{ GeV}/c$  and rapidity  $|y| < 0.5$  and take the average over the multiplicity of the  $\Lambda$  particles. We begin by comparing the percentage value of  $\overline{\mathcal{R}}_\Lambda^t$  for the four usual types of vorticity: kinetic, thermal, kinetic with spacial projection and temperature. This is shown on Fig. 5.12, and the similarities between the kinetic, thermal and temperature vorticities implies that vorticity is caused mainly by the velocity gradients, not by the correspondingly temperature factor in their definitions. The fact that the spacial projection vorticity curve is bigger than the others shows that the acceleration components of the thermal, kinetic and temperature vorticity lowers the value of  $\overline{\mathcal{R}}_\Lambda^t$ . We also study the response of the  $\overline{\mathcal{R}}_\Lambda^t$  value to variations on the shear viscosity of the medium. In Fig. 5.13 we analyse values of  $\eta/s = 0, 0.01, 0.08, 0.16$  and  $0.24$ , observing that the ring parameter increases for lower viscosities, which is consistent with the idea of the vorticity of the jet diminishing in a more viscous medium.

Finally, we consider a scenario where both components of the dijet are thermalized in the fluid. In Fig. 5.14 we show three different possibilities: two superimposed

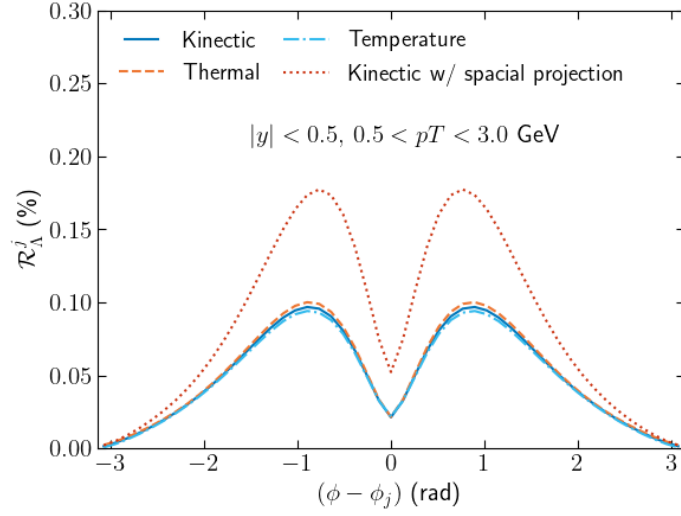


Figure 5.12:  $\overline{\mathcal{R}}_{\Lambda}^{\hat{t}}$  parameter comparison for different types of vorticity. The  $y$  axis represents the percentage of the observable  $\overline{\mathcal{R}}_{\Lambda}^{\hat{t}}$  and the  $x$  axis the azimuthal angle relative to the jet direction. The similar values of  $\overline{\mathcal{R}}_{\Lambda}^{\hat{t}}$  for the thermal, kinetic, and temperature vorticities indicate that the vorticity is formed, mainly, by gradients of velocity.

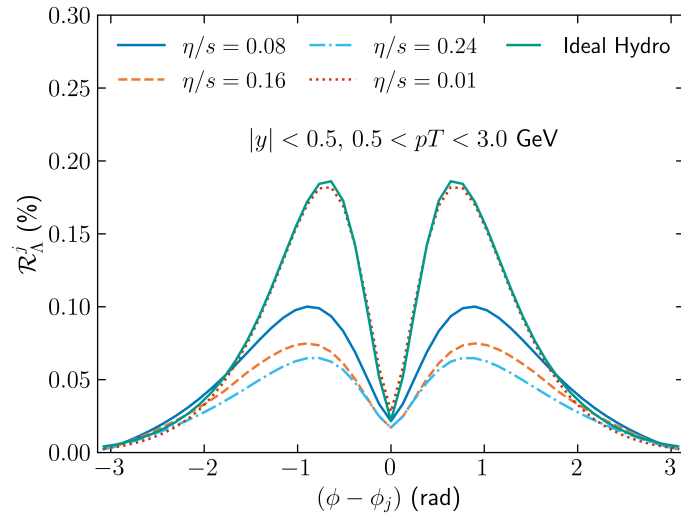


Figure 5.13:  $\overline{\mathcal{R}}_{\Lambda}^{\hat{t}}$  parameter comparison for different values of shear viscosity. The  $y$  axis represents the percentage of the observable  $\overline{\mathcal{R}}_{\Lambda}^{\hat{t}}$  and the  $x$  axis the azimuthal angle relative to the jet direction. We see that the increase in the viscosity also interferes in the values of  $\overline{\mathcal{R}}_{\Lambda}^{\hat{t}}$ , and consequently, in the polarization of  $\Lambda$ .

quenched jets moving in opposite directions (red dashed curve); a double quenched jet, with one jet located at  $x = 0.6$  fm and the other at  $x = -0.6$  fm with opposite momentum (blue curve); and the usual single quenched jet, placed at the origin. We observe that the hydrodynamic response of the medium in the back-to-back dijet scenario is that of

shifting the  $\overline{\mathcal{R}}_{\Lambda}^i$  to the negative and opposite direction while maintaining a similar value of the singled quenched jet for the forward direction. Also, when we compare the blue curve with the red curve we observe a slight drop in the polarization value, indicating that the turbulence caused by the jet in the opposite direction decreases the polarization value of the jet in the  $+x$  direction.

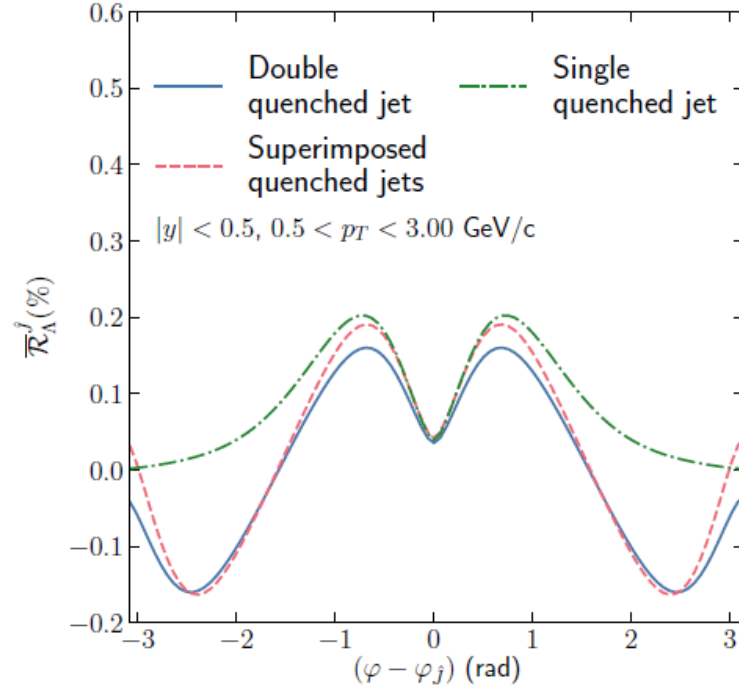


Figure 5.14:  $\overline{\mathcal{R}}_{\Lambda}^i$  parameter comparison for different jet thermalization scenarios as a function of the azimuthal angle relative to the jet direction. The green curve shows the case where there's only one jet travelling in the  $+x$  direction. The red curve describes the behavior of two superimposed jets, moving at opposite directions. The blue curve shows the scenario where two jets are separated by a distance  $\Delta x = 1.2$  fm in the  $x$  axis, also moving in opposite directions.

## Final Considerations

In this work we showed that the  $\Lambda$  polarization is a powerful tool that allows the exploration of the properties of the Quark-Gluon Plasma. Through viscous hydrodynamic simulations, we were able to establish a direct relation between a physical observable and the properties of a relativistic fluid, believed to be created in the relativistic heavy-ion collision. We modeled the effect of the jet thermalization inside the QGP as a region of higher energy density and momentum placed on top of a smooth initial condition. With this configuration we showed that the  $\overline{\mathcal{R}}_{\Lambda}^i$  observable, which encodes the information of polarization of the Lambda hyperons, is affected to variations in the properties of the fluid. We studied its response to different values of shear viscosity to entropy ratio  $\eta/s$ , and to different definitions of vorticity. The similarities between the  $\overline{\mathcal{R}}_{\Lambda}^i$  definitions using the kinetic, thermal and temperature dependent vorticity show that the vorticity is mostly generated by velocity gradients. At last, we studied a more realistic approach where two components of a dijet are quenched in the QGP. In this case, the main effect is that of lowering the values of  $\overline{\mathcal{R}}_{\Lambda}^i$  in the opposite direction when compared to the single quenched jet.

In our model, the thermalized jet moves in the  $+x$  direction, with initial energy  $\epsilon V = 30$  GeV and velocity  $v_x = 0.7c$ . This configuration was evolved using a (3+1)D hydrodynamic code. We observed that the energy and momentum deposited by the thermalization propagation introduces velocity gradients into the medium, creating a vortex ring that can be described in terms of the vorticity of the fluid. We do a systematic study in order to understand the consequences of the jet passing through the relativistic fluid. We analyse the energy density, the vorticity profiles of the fluid evolution, and their dependence on the variation of specific viscosity. From these analysis we note that energy

and vorticity behaviour vary directly with the  $\eta/s$ , dissipating faster for a more viscous medium.

We see a direct dependence between the average  $z$ -component of the vorticity at the freeze-out hypersurface and the polarization of  $\Lambda$  particles, indicating that this polarization inherits the physical properties of the fluid. Also, the  $z$  component of this polarization tends to be maximum around the direction of the emitted particles.

As commented before, the results shown in this work are important in the sense that they connect a physical measurement, the polarization of the Lambda hyperon, to the properties of a strongly coupled matter formed by deconfined quarks and gluons. In this context, if experiments show that polarization is formed around the jet passing through QGP, this would be a confirmation that the jet is indeed thermalized in the fluid. This confirmation would also imply that the jet interacts directly with the QGP and that the polarization is an observable that can possibly probe the properties of this relativistic matter.

---

# Bibliography

---

- <sup>1</sup>U. Heinz and R. Snellings, “Collective flow and viscosity in relativistic heavy-ion collisions”, [Annual Review of Nuclear and Particle Science](#) **63**, 123–151 (2013).
- <sup>2</sup>P. Romatschke and U. Romatschke, *Relativistic fluid dynamics in and out of equilibrium – ten years of progress in theory and numerical simulations of nuclear collisions*, 2019.
- <sup>3</sup>“Global  $\Lambda$  hyperon polarization in nuclear collisions”, [Nature](#) **548**, 62–65 (2017).
- <sup>4</sup>*Proceedings of the 15th international conference on ultrarelativistic nucleus-nucleus collisions (qm 2001)* (Stony Brook, New York, January 15-20, Nucl. Phys. A 698 (2002), 2001).
- <sup>5</sup>*Proceedings of the 16th international conference on ultrarelativistic nucleus-nucleus collisions (qm 2002)* (Nantes, France, July 18-24, Nucl. Phys. A 715 (2003), 2002).
- <sup>6</sup>J. Adams, M. Aggarwal, Z. Ahammed, J. Amonett, B. Anderson, D. Arkhipkin, G. Averichev, S. Badyal, Y. Bai, J. Balewski, and et al., “Experimental and theoretical challenges in the search for the quark–gluon plasma: the star collaboration’s critical assessment of the evidence from rhic collisions”, [Nuclear Physics A](#) **757**, 102–183 (2005).
- <sup>7</sup>K. M. O’Hara, S. L. Hemmer, M. E. Gehm, S. R. Granade, and J. E. Thomas, “Observation of a strongly interacting degenerate fermi gas of atoms”, [Science](#) **298**, 2179–2182 (2002).
- <sup>8</sup>X.-N. Wang, “30 years of jet quenching”, [PoS High-pT2019](#), 040 (2020).
- <sup>9</sup>J. D. Bjorken, “Energy Loss of Energetic Partons in Quark - Gluon Plasma: Possible Extinction of High  $p(t)$  Jets in Hadron - Hadron Collisions”, (1982).
- <sup>10</sup>U. A. Wiedemann, “Jet quenching in heavy ion collisions”, [Landolt-Börnstein - Group I Elementary Particles, Nuclei and Atoms](#), 521–562 (2010).

- <sup>11</sup>A. Majumder and M. van Leeuwen, “The theory and phenomenology of perturbative qcd based jet quenching”, *Progress in Particle and Nuclear Physics* **66**, 41–92 (2011).
- <sup>12</sup>P. Kurt (ATLAS, CMS), “Jet Quenching with ATLAS and CMS”, *EPJ Web Conf.* **66**, edited by S. Lunardi, P. G. Bizzeti, C. |. Bucci, M. Chiari, A. Dainese, P. Di Nezza, R. Menegazzo, A. Nannini, C. Signorini, and J. J. Valiente-Dobon, 04017 (2014).
- <sup>13</sup>V. K. et al (CMS Collaboration), “Measurement of inclusive jet cross sections in  $pp$  and pbb collisions at  $\sqrt{s_{NN}} = 2.76$  tev”, *Phys. Rev. C* **96**, 015202 (2017).
- <sup>14</sup>J. Casalderrey-Solana and C. A. Salgado, *Introductory lectures on jet quenching in heavy ion collisions*, 2007.
- <sup>15</sup>D. d’Enterria, “6.4 jet quenching”, *Landolt-Börnstein - Group I Elementary Particles, Nuclei and Atoms*, 471–520 (2010).
- <sup>16</sup>B. Back, M. Baker, M. Ballintijn, D. Barton, B. Becker, R. Betts, A. Bickley, R. Bindel, A. Budzanowski, W. Busza, and et al., “The phobos perspective on discoveries at rhic”, *Nuclear Physics A* **757**, 28–101 (2005).
- <sup>17</sup>S. Salur, “First direct measurement of jets in  $\sqrt{s_{NN}} = 200$  GeV heavy ion collisions by star”, *The European Physical Journal C* **61**, 761–767 (2009).
- <sup>18</sup>D. A. Appel, “Jets as a probe of quark-gluon plasmas”, *Phys. Rev. D* **33**, 717–722 (1986).
- <sup>19</sup>J. P. Blaizot and L. D. McLerran, “Jets in expanding quark-gluon plasmas”, *Phys. Rev. D* **34**, 2739–2745 (1986).
- <sup>20</sup>J. A. et al. (STAR Collaboration), “Evidence from d+au measurements for final-state suppression of high- $p_T$  hadrons in Au+Au collisions at rhic”, *Phys. Rev. Lett.* **91**, 072304 (2003).
- <sup>21</sup>A. Gadomski, “Addressing nanoscale soft-matter problems by computational physics and physical computation – an example of facilitated lubrication in a two-surface system with hydrodynamic interlayer (with wieslaw urbaniak and roland g. winkler) pp. 33-34. recognizing an applied-physics and physicochemical succession of jan czochralski, an outstanding european crystal grower and personality (with jan klos) 35-36”, in (June 2015).
- <sup>22</sup>M. Thomson, *Modern particle physics*, Modern Particle Physics (Cambridge University Press, 2013).

- <sup>23</sup>W. Commons, *File:giant smoke ring.jpg — wikimedia commons, the free media repository*, 2020.
- <sup>24</sup>Z.-T. Liang and X.-N. Wang, “Globally polarized quark-gluon plasma in noncentral  $A+A$  collisions”, *Physical Review Letters* **94**, [10.1103/physrevlett.94.102301](https://doi.org/10.1103/physrevlett.94.102301) (2005).
- <sup>25</sup>F. Becattini and M. A. Lisa, “Polarization and vorticity in the quark–gluon plasma”, *Annual Review of Nuclear and Particle Science* **70**, 395–423 (2020).
- <sup>26</sup>W. M. Serenone, J. G. P. Barbon, D. D. Chinellato, M. A. Lisa, C. Shen, J. Takahashi, and G. Torrieri, “A Polarization from thermalized jet energy”, *Physics Letters B* **820**, 136500 (2021).
- <sup>27</sup>M. A. Lisa, J. G. Prado Barbon, D. D. Chinellato, W. M. Serenone, C. Shen, J. Takahashi, and G. Torrieri, “Vortex rings from high energy central p+a collisions”, *Physical Review C* **104**, [10.1103/physrevc.104.1011901](https://doi.org/10.1103/physrevc.104.1011901) (2021).
- <sup>28</sup>B. Schenke, S. Jeon, and C. Gale, “(3+1)d hydrodynamic simulation of relativistic heavy-ion collisions”, *Physical Review C* **82**, [10.1103/physrevc.82.014903](https://doi.org/10.1103/physrevc.82.014903) (2010).
- <sup>29</sup>J. E. Bernhard, *Bayesian parameter estimation for relativistic heavy-ion collisions*, 2018.
- <sup>30</sup>J. C. Collins and M. J. Perry, “Superdense matter: neutrons or asymptotically free quarks?”, *Phys. Rev. Lett.* **34**, 1353–1356 (1975).
- <sup>31</sup>A. D. Linde, “Phase transitions in gauge theories and cosmology”, **42**, 389–437 (1979).
- <sup>32</sup>R. Furnstahl and J. Steele, *Expansion of the universe*, 1997,1998.
- <sup>33</sup>T. Sasaki, N. Yasutake, M. Kohno, H. Kouno, and M. Yahiro, *Determination of quark-hadron transition from lattice qcd and neutron-star observation*, 2013.
- <sup>34</sup>P. Steinbrecher, “The qcd crossover at zero and non-zero baryon densities from lattice qcd”, *Nuclear Physics A* **982**, 847–850 (2019).
- <sup>35</sup>A. Aduszkiewicz, Y. Ali, E. Andronov, T. Antićić, B. Baatar, M. Baszczyk, S. Bhosale, A. Blondel, M. Bogomilov, A. Brandin, and et al., “Measurements of  $\pi^\pm$ ,  $K^\pm$ , p and  $\bar{p}$  spectra in proton-proton interactions at 20, 31, 40, 80 and 158 GeV /c with the na61/shine spectrometer at the cern sps”, *The European Physical Journal C* **77**, [10.1140/epjc/s10052-017-5260-4](https://doi.org/10.1140/epjc/s10052-017-5260-4) (2017).
- <sup>36</sup>X. Luo, “Exploring the qcd phase structure with beam energy scan in heavy-ion collisions”, *Nuclear Physics A* **956**, 75–82 (2016).

- <sup>37</sup>A. Bzdak, S. Esumi, V. Koch, J. Liao, M. Stephanov, and N. Xu, “Mapping the phases of quantum chromodynamics with beam energy scan”, *Physics Reports* **853**, 1–87 (2020).
- <sup>38</sup>H.-T. Ding, F. Karsch, and S. Mukherjee, *Thermodynamics of strong-interaction matter from lattice qcd*, 2015.
- <sup>39</sup>R. Snellings, “Elliptic flow: a brief review”, *New Journal of Physics* **13**, 055008 (2011).
- <sup>40</sup>J. D. Bjorken, “Highly relativistic nucleus-nucleus collisions: the central rapidity region”, *Phys. Rev. D* **27**, 140–151 (1983).
- <sup>41</sup>R. L. Ray and M. S. Daugherty, “Applicability of monte carlo glauber models to relativistic heavy-ion collision data”, *Journal of Physics G: Nuclear and Particle Physics* **35**, 125106 (2008).
- <sup>42</sup>P. Braun-Munzinger and B. Dönigus, “Loosely-bound objects produced in nuclear collisions at the lhc”, *Nuclear Physics A* **987**, 10.1016/j.nuclphysa.2019.02.006 (2019).
- <sup>43</sup>L. D. Landau, “On the multiparticle production in high-energy collisions”, *Izv. Akad. Nauk Ser. Fiz.* **17**, 51–64 (1953).
- <sup>44</sup>D. Kharzeev, “Important experimental observables at RHIC”, *Nucl. Phys. A* **715**, edited by H. Gutbrod, J. Aichelin, and K. Werner, 35–44 (2003).
- <sup>45</sup>H. Gutbrod, J. Aichelin, and K. Werner, eds., *Proceedings, 16th International Conference on Ultra-Relativistic nucleus nucleus collisions (Quark Matter 2012): Nantes, France, July 18-24, 2002*, Vol. 715 (2003), pp.1–930.
- <sup>46</sup>L. Euler, *Principes généraux du mouvement des fluides*, 1757.
- <sup>47</sup>L. Landau and E. Lifshitz, *Fluid mechanics: volume 6*, v. 6 (Elsevier Science, 2013).
- <sup>48</sup>C. Navier, *Mémoire sur les lois du mouvement des fluides* (1827), 6:389–440.
- <sup>49</sup>G. G. Stokes, “On the theories of the internal friction of fluids in motion, and of the equilibrium and motion of elastic solids”, in *Mathematical and physical papers*, Vol. 1, Cambridge Library Collection - Mathematics (Cambridge University Press, 2009), pp. 75–129.
- <sup>50</sup>M. Schwartz, *Quantum field theory and the standard model*, Quantum Field Theory and the Standard Model (Cambridge University Press, 2014).
- <sup>51</sup>P. K. Kovtun, D. T. Son, and A. O. Starinets, “Viscosity in strongly interacting quantum field theories from black hole physics”, *Phys. Rev. Lett.* **94**, 111601 (2005).

- <sup>52</sup>M. Luzum and J.-Y. Ollitrault, “Extracting the shear viscosity of the quark-gluon plasma from flow in ultra-central heavy-ion collisions”, *Nuclear Physics A* **904-905**, 377c–380c (2013).
- <sup>53</sup>G. S. Denicol, T. Kodama, T. Koide, and P. Mota, “Effect of bulk viscosity on elliptic flow near the qcd phase transition”, *Phys. Rev. C* **80**, 064901 (2009).
- <sup>54</sup>A. Monnai and T. Hirano, “Effects of bulk viscosity at freezeout”, *Phys. Rev. C* **80**, 054906 (2009).
- <sup>55</sup>H. Song and U. Heinz, “Interplay of shear and bulk viscosity in generating flow in heavy-ion collisions”, *Phys. Rev. C* **81**, 024905 (2010).
- <sup>56</sup>K. Paech and S. Pratt, “Origins of bulk viscosity in relativistic heavy ion collisions”, *Phys. Rev. C* **74**, 014901 (2006).
- <sup>57</sup>S. A. Voloshin and T. Niida, “Ultrarelativistic nuclear collisions: direction of spectator flow”, *Physical Review C* **94**, 021901 (2016).
- <sup>58</sup>S. A. Voloshin, “Vorticity and particle polarization in heavy ion collisions (experimental perspective)”, *EPJ Web of Conferences* **171**, edited by A. Mischke and P. Kuijser, 07002 (2018).
- <sup>59</sup>J. Adam et al. (STAR Collaboration), “Global polarization of  $\Lambda$  hyperons in au + au collisions at  $\sqrt{s_{NN}} = 200$  gev”, *Phys. Rev. C* **98**, 014910 (2018).
- <sup>60</sup>M. Anderson, J. Berkovitz, W. Betts, R. Bossingham, F. Bieser, R. Brown, M. Burks, M. Calderón de la Barca Sánchez, D. Cebra, M. Cherney, and et al., “The star time projection chamber: a unique tool for studying high multiplicity events at rhic”, *Nuclear Instruments and Methods in Physics Research Section A: Accelerators, Spectrometers, Detectors and Associated Equipment* **499**, 659–678 (2003).
- <sup>61</sup>X. Dong, “The time-of-flight detector for rhic/star and the related physics”, **865**, 10.1063/1.2398870 (2006).
- <sup>62</sup>E. Alpatov, “Global hyperon polarization in au+au collisions at  $\sqrt{s_{NN}} = 27$  gev in the STAR experiment”, *Journal of Physics: Conference Series* **1690**, 012120 (2020).
- <sup>63</sup>L. G. Pondrom, “Hyperon experiments at fermilab”, **122**, 57–172 (1985).
- <sup>64</sup>E. Speranza and N. Weickgenannt, *Spin tensor and pseudo-gauges: from nuclear collisions to gravitational physics*, June 2020.

- <sup>65</sup>X.-L. Xia, H. Li, X.-G. Huang, and H. Z. Huang, “Feed-down effect on  $\Lambda$  spin polarization”, *Phys. Rev. C* **100**, 014913 (2019).
- <sup>66</sup>T. D. Lee and C. N. Yang, “General partial wave analysis of the decay of a hyperon of spin 1/2.”, **108**, 1645–1647 (1957).
- <sup>67</sup>M. Tanabashi et al., “Review of particle physics”, **98**, 030001 (2018).
- <sup>68</sup>I. Upsal, “Observation of global hyperon polarization in ultrarelativistic heavy ion collisions”, **736**, 012016 (2016).
- <sup>69</sup>A. M. Poskanzer and S. A. Voloshin, “Methods for analyzing anisotropic flow in relativistic nuclear collisions”, **58**, 1671–1678 (1998).
- <sup>70</sup>B. I. Abelev et al. (STAR Collaboration), “Global polarization measurement in au+au collisions”, *Phys. Rev. C* **76**, 024915 (2007).
- <sup>71</sup>F. Becattini, G. Inghirami, V. Rolando, A. Beraudo, L. D. Zanna, A. D. Pace, M. Nardi, G. Pagliara, and V. Chandra, “A study of vorticity formation in high energy nuclear collisions”, *The European Physical Journal C* **75**, <https://doi.org/10.1140/epjc/s10052-015-3624-1> (2015).
- <sup>72</sup>M. A. Lisa, J. G. P. Barbon, D. D. Chinellato, W. M. Serenone, C. Shen, J. Takahashi, and G. Torrieri, *Vortex rings from high energy central p+a collisions*, 2021.
- <sup>73</sup>W. Ke, J. S. Moreland, J. E. Bernhard, and S. A. Bass, “Constraints on rapidity-dependent initial conditions from charged-particle pseudorapidity densities and two-particle correlations”, *Physical Review C* **96**, [10.1103/physrevc.96.044912](https://doi.org/10.1103/physrevc.96.044912) (2017).
- <sup>74</sup>G. Aad, B. Abbott, J. Abdallah, A. A. Abdelalim, A. Abdesselam, O. Abdinov, B. Abi, M. Abolins, H. Abramowicz, H. Abreu, and et al., “Observation of a centrality-dependent dijet asymmetry in lead-lead collisions at  $\sqrt{s_{NN}} = 2.76$  tev with the atlas detector at the lhc”, *Physical Review Letters* **105**, [10.1103/physrevlett.105.252303](https://doi.org/10.1103/physrevlett.105.252303) (2010).
- <sup>75</sup>M. Aaboud, G. Aad, B. Abbott, J. Abdallah, O. Abdinov, B. Abeloos, S. Abidi, O. AbouZeid, N. Abraham, H. Abramowicz, and et al., “Measurement of jet pt correlations in pb+pb and pp collisions at  $\sqrt{s_{NN}} = 2.76$  tev with the atlas detector”, *Physics Letters B* **774**, 379–402 (2017).
- <sup>76</sup>H. Li, L.-G. Pang, Q. Wang, and X.-L. Xia, “Global  $\Lambda$  polarization in heavy-ion collisions from a transport model”, *Physical Review C* **96**, [10.1103/physrevc.96.054908](https://doi.org/10.1103/physrevc.96.054908) (2017).

- <sup>77</sup>G. S. Denicol, H. Niemi, E. Molnár, and D. H. Rischke, “Derivation of transient relativistic fluid dynamics from the boltzmann equation”, [Physical Review D \*\*85\*\*, 10.1103/physrevd.85.114047 \(2012\)](#).
- <sup>78</sup>E. Molnár, H. Niemi, G. Denicol, and D. Rischke, “Relative importance of second-order terms in relativistic dissipative fluid dynamics”, [Physical Review D \*\*89\*\*, 10.1103/physrevd.89.074010 \(2014\)](#).
- <sup>79</sup>R. Soltz, “The hotqcd equation of state”, [Nuclear Physics A \*\*830\*\*, 725c–728c \(2009\)](#).
- <sup>80</sup>C. Shen, Z. Qiu, H. Song, J. Bernhard, S. Bass, and U. Heinz, *The iebe-vishnu code package for relativistic heavy-ion collisions*, 2015.
- <sup>81</sup>F. Cooper and G. Frye, “Single-particle distribution in the hydrodynamic and statistical thermodynamic models of multiparticle production”, [Phys. Rev. D \*\*10\*\*, 186–189 \(1974\)](#).

---

**APPENDIX A**

---

**$\Lambda$  polarization from thermalized jet  
energy**

---

## A polarization from thermalized jet energy

Willian Matioli Serenone<sup>a,\*</sup>, João Guilherme Prado Barbon<sup>a</sup>, David Dobrigkeit Chinellato<sup>a</sup>, Michael Annan Lisa<sup>b</sup>,  
Chun Shen<sup>c,d</sup>, Jun Takahashi<sup>a</sup>, Giorgio Torrieri<sup>a</sup>

<sup>a</sup>*Instituto de Física Gleb Wataghin, Universidade Estadual de Campinas, Campinas, Brasil*

<sup>b</sup>*The Ohio State University, Columbus, Ohio, USA*

<sup>c</sup>*Department of Physics and Astronomy, Wayne State University, Detroit, MI 48201, USA*

<sup>d</sup>*RIKEN BNL Research Center, Brookhaven National Laboratory Upton, NY 11973, USA*

---

### Abstract

We examine the formation of vortical “smoke rings” as a result of thermalization of energy lost by a jet. We simulate the formation and evolution of these rings using hydrodynamics and define an observable that allows to probe this phenomenon experimentally. We argue that observation of vorticity associated with jets would be an experimental confirmation of the thermalization of the energy lost by quenched jets, and also a probe of shear viscosity.

### 1. Introduction

Two of the most studied results in heavy ion physics at ultra-relativistic energies are jet energy loss [1, 2, 3, 4, 5] and fluid behavior [6, 7, 8, 9, 10, 11]. The first shows that colored degrees of freedom form “a medium” opaque to fast partons, and the second shows this medium thermalizes very quickly and subsequent evolution is nearly inviscid. Both results are usually interpreted as evidence that the medium created in heavy ion collisions is a “strongly coupled liquid”.

However, considerable theoretical uncertainty exists regarding the fate of the energy lost by the jet. If the plasma is a very good fluid it is a reasonable hypothesis that the jet energy should thermalize and contribute to the fluid flow gradients. However, we do not have a clear experimental signature of this. Partially, this is because the models of parton-medium interaction are inconclusive [12], and partially it is because direct signatures of fluid behavior, such as “Conical flow”, have not been conclusively observed [13, 14].

Recently, a new intriguing manifestation of hydrodynamic behavior has been found: A polarization, measurable via parity violating decays [15]. It seems to be aligned to the global vorticity of the fluid and, to an extent, with near-ideal hydrodynamic vorticity being transferred into Polarization via an isentropic transition, respecting angular momentum conservation [16]. As well as a further confirmation of the fluid-like behav-

ior of the medium, this observation opens the door to use polarization as a tool to study the medium’s dynamics.

We propose to use polarization to understand the fate of locally thermalized energy emitted by the jet. A schematic picture of the physical situation is shown in Fig. 1. A hard parton generates a dijet structure and one of these is partially quenched by the quark-gluon plasma, while the other is not. The quenched portion of the jet introduces a initial velocity gradient in the fluid. As is known from everyday physics, smoke-rings, eddies and so on are ubiquitous in fluids when a velocity gradient is present. This is certainly the case when a fast parton deposits energy into a medium. The only difficulty is, of course, that the jet’s direction fluctuates event-by-event which vanishes after the event averaging.

This is, however, easily surmountable: As argued in [17], the interplay between vorticity and transverse expansion can be used to define a “jet production plane”. This insight can be sharpened into the definition of an experimental observable that ties the polarization direction, the angular momentum and a desired reference vector, which can be defined event-by-event. In this work, we shall focus on defining the reference vector as a high- $p_T$  trigger particle. This observable, if measured to be non-zero in classes of events where jet suppression exists, would provide unique and compelling evidence that the energy lost by the jet is indeed thermalized. Moreover, it can be used to infer the medium’s viscosity, provided the initial velocity gradients generated by the jet are quantified.

---

\*Corresponding author

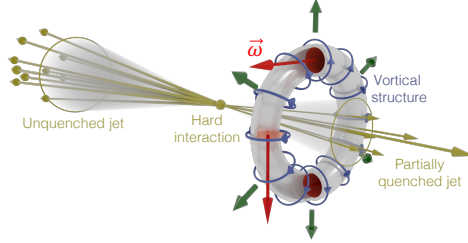


Figure 1: Schematic representation of the physical situation proposed. A hard parton generates a dijet structure and one of these jets is partially quenched by the quark-gluon plasma, while the other is not. The quenched portion of the jet introduces a momentum gradient in the fluid which in turn will generate a vortex ring.

## 2. A model for the jet thermalization

Our first step is to choose a suitable model for the medium in which the jet will deposit (part of) its energy. We choose a model which incorporates three dimensional features, since the  $\Lambda$  polarization calculation we will perform later on will depend on the dynamics in all dimensions. The need to perform (3+1)D simulation imposes a heavy computational constraint. To make our work feasible, we take the average over a thousand initial conditions, generated with T<sub>R</sub>ENTo 3D [18] configured for simulations of Pb–Pb collisions at  $\sqrt{s_{NN}} = 2.76$  TeV, all of them with impact parameter  $b = 0$  fm. The other parameters used to generate these initial conditions were obtained from Ref. [19] (for parameters common to 2D and 3D T<sub>R</sub>ENTo) and Ref. [18] (for parameters exclusive to 3D T<sub>R</sub>ENTo). These are summarized in Table 1. All computations are made in a grid with spacing equal to 0.1 fm in the  $x$  and  $y$  directions<sup>1</sup> and 0.2 in the spatial rapidity ( $\eta_s$ ) direction.

We expect the event-averaged fluid background to give a good estimation on the polarization final observable. Karpenko and Becattini [20] showed that the difference between event-by-event simulations and an averaged initial condition to be small, albeit the source of  $\Lambda$  polarization in their work is different from ours.

Now we turn our attention to the jet thermalization. We consider a scenario of dijet creation inside the medium, where one jet will lose a negligible amount of energy and momentum while the other will be partially quenched, causing an asymmetry in jet emission. This

<sup>1</sup>We attempted halving the grid spacing in  $x$  and  $y$  directions and our main results changed by only 1%, at the expense of a much greater computational effort.

Table 1: Input parameters for T<sub>R</sub>ENTo 3D.

Parameter	Value
Rapidity mean coefficient	0.0
Rapidity standard coefficient	2.9
Rapidity skewness coefficient	7.3
Skewness type	Relative skewness
Jacobian	0.75
Reduced thickness	0.007
Nucleon width	0.956 fm
Nucleon minimum distance	1.27 fm

is measured experimentally using the jet asymmetry observables  $A_J$  and  $x_J$ , defined as [4, 21, 22, 23]

$$x_J \equiv p_{T_2}/p_{T_1}, \quad (1)$$

$$A_J \equiv (E_{T_1} - E_{T_2})/(E_{T_2} + E_{T_1}). \quad (2)$$

The index “1” denote the trigger jet (the one that does not deposit energy and momentum in the medium) while the index “2” refers to the partially quenched jet.

From Eqs. (1) and (2), one can obtain the momentum (energy) of the quenched jet from the values of  $x_J$  ( $A_J$ ) and the momentum (energy) of the trigger jet. Once  $E_{T_2}$  and  $p_{T_2}$  are determined, one may get the energy and momentum deposited in the medium as

$$\begin{aligned} p_{th} &= p_{T_1} - p_{T_2}, \\ E_{th} &= E_{T_1} - E_{T_2}. \end{aligned} \quad (3)$$

We will use the data from [4, Fig. 3] and [22, Fig. 8] to determine the values of  $p_{th}$  and  $E_{th}$ . These are the distribution of  $dN/dA_J$  and  $dN/dx_J$  for central Pb–Pb collisions at  $\sqrt{s_{NN}} = 2.76$  TeV. The energy and momentum of the trigger jet in these measurements were  $E_1 > 100$  GeV and  $p_{T_1} = 89.5$  GeV/ $c$ . For the values of  $A_J$  and  $x_J$ , we choose the ones that have the highest value of multiplicity, i.e.  $A_J = 0.425$  and  $x_J = 0.525$ . This gives us  $E_{th} = 59.6$  GeV and  $p_{th} = 43$  GeV/ $c$ . This implies that the situation studied in what follows corresponds to a dijet structure with a momentum of 89.5 GeV/ $c$  for the unquenched jet and 59.5 GeV/ $c$  for the partially quenched jet, noting that it is the latter that defines the direction in which lambda polarization will be studied.

The measurements that will be proposed later will be shown as a function of the difference between the azimuthal angle of the partially quenched jet and the emitted  $\Lambda$ . For simplicity, we choose the jet in the  $x$ -direction without loss of generality. With this choice, we may write the thermalized four-momentum as  $p_{th}^\mu = (E_{th} \ p_{th} \ 0 \ 0)$  and build an

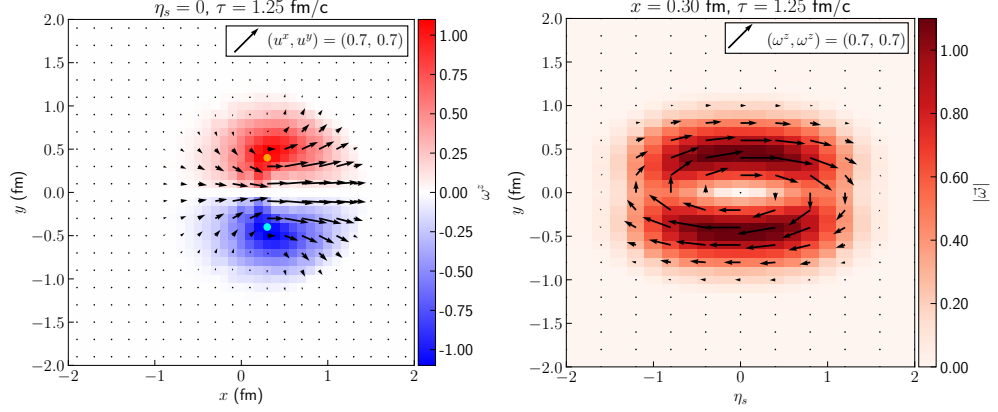


Figure 2: Vortex ring formed by the thermalized jet after  $\Delta\tau = 1.00$  fm/c of hydrodynamic evolution. The jet deposited momentum in the  $\hat{x}$  direction, i.e. to the right in the left panel and away from the viewer in the right panel. In the left panel, it is shown a slice of the system at  $\eta_s = 0$ . The color map shows the  $z$ -component of vorticity vector defined in Eq. (8). The arrows shows the  $x$  and  $y$  components of the fluid's four-velocities. The dots marks the local maxima of  $|\omega^z|$ . On the right panel, the system is sliced along the position  $x = 0.3$  fm. The color map shows  $|\vec{\omega}|$  and the arrows shows the  $y$  and  $z$  components of the vorticity vector.

energy-momentum tensor  $T^{\mu\nu}$  following

$$T^{\mu\nu} = \frac{1}{V} \frac{P_{th}^\mu P_{th}^\nu}{E_{th}}, \quad (4)$$

where  $V$  is the volume over which the energy and momentum is deposited. The volume is chosen to be an oblate spheroid centered on the origin of the system, with axis size equal to 0.5 fm in the  $x$  and  $y$  directions and  $\approx 0.29$  fm in the  $z$ -direction (which equates to  $\eta_s \approx 1$  at  $\tau = 0.25$  fm/c).

We apply the Landau matching procedure  $T^{\mu\nu}u_\nu = \varepsilon u^\mu$  to solve for the local energy density and flow velocity from the energy-momentum tensor in Eq. (4)

$$\varepsilon = \frac{1}{V} \frac{E_{th}^2 - P_{th}^2}{E_{th}}, \quad (5)$$

$$u^x = \frac{P_{th}}{\sqrt{E_{th}^2 - P_{th}^2}}. \quad (6)$$

The remaining spatial components of  $u^\mu$  are zero and  $u^\tau$  is obtained by imposing the condition  $u^\mu u_\mu = 1$ . This procedure (energy-momentum tensor building and subsequent matching to a hydrodynamic-like energy-momentum tensor) was inspired by the procedure used for computing vorticity generated in the AMPT model in Ref. [24].

By inserting in Eqs. (5) and (6) the values for  $E_{th}$  and  $P_{th}$  obtained above, we obtain  $\varepsilon V = 29$  GeV and

$v_x = 0.69 c$ , where  $V$  is the volume over which the energy density will be deposited. In our simulations, we rounded these values to  $\varepsilon V = 30$  GeV and  $v_x = 0.7 c$ . We verified that the injected energy-momentum generates on average 1% more final state particles per unit of pseudo-rapidity.

### 3. Fluid vorticity and polarization measurements

#### 3.1. Jet induced fluid vorticity and $\Lambda$ 's polarization

The described initial condition is evolved with 3D viscous hydrodynamics [25, 26, 27]. We use the lattice-QCD based equation of state from the HotQCD Collaboration [28] and start the evolution at  $\tau = 0.25$  fm/c. The six independent components of the vorticity tensor are then saved over a hypersurface of  $T = 151$  MeV. We then compute the mean spin of  $\Lambda$  following Eq. (2) of Ref. [15], which we reproduce below for completeness.

$$P^\mu(p) = -\frac{1}{8m} \varepsilon^{\mu\rho\sigma\tau} p_\tau \frac{\int d\Sigma_\lambda p^\lambda n_F (1 - n_F) \omega_{\rho\sigma}}{\int d\Sigma_\lambda p^\lambda n_F}, \quad (7)$$

$$n_F = \frac{1}{1 + \exp(\beta^\mu p_\mu - \mu Q/T)},$$

$$\omega^{\mu\nu} = -\frac{1}{2} (\partial^\mu \beta^\nu - \partial^\nu \beta^\mu) \quad \text{and} \quad \beta^\mu = \frac{u^\mu}{T}.$$

In our case, we do not consider baryon density and baryon currents and thus  $\mu = 0$  MeV.

With the six components of the vorticity tensor  $\omega^{\mu\nu}$  we calculate a vorticity vector  $\omega^\mu$  (inspired on the Pauli–Lubanski pseudovector), which will act as a proxy for the local spin polarization,

$$\omega^\mu \equiv \varepsilon^{\mu\nu\rho\epsilon} u_\nu \omega_{\rho\epsilon}. \quad (8)$$

In Figure 2, we show the spatial distributions of  $\omega^z$  (along a slice of  $\eta_s = 0$ ) and  $|\vec{\omega}|$  (along a slice of  $x = 0.3$  fm) at  $\tau = 1.25$  fm/c. The external energy-momentum from the jet induces a ring-shaped concentration of vorticity around the jet axis during the hydrodynamic evolution.

To verify the vortical structures in the fluid velocity field are mapped to the spin polarization of emitted  $\Lambda$ , we compare the averaged  $\omega^z$  on the particlization hypersurface in the region  $|\eta_s| < 0.5$  with the  $\Lambda$ 's  $P^z$ , averaged over the region  $|y| < 0.5$  and  $p_T < 3.0$  GeV/c in Fig. 3. To obtain the azimuthal angle of each cell on the particlization hypersurface, we use the cell's four-velocity, i.e.  $\varphi = \arctan(u^y/u^x)$ . Since the fluid is expanding in a mostly radial way, the velocity angle  $\varphi$  is close to the spatial azimuthal angle of the cell. Figure 3 shows that the sign of  $\Lambda$  polarization correlates well with that of the fluid vorticity vector  $\omega^\mu$  in Eq. (8).

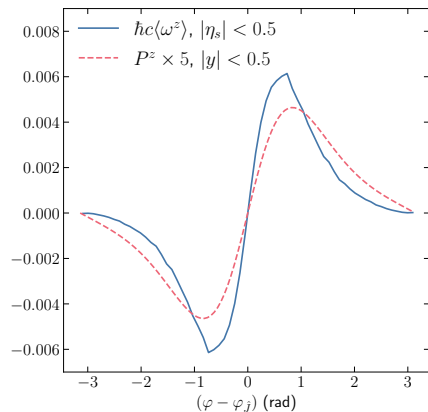


Figure 3: Comparison between the weighted average of the  $z$ -component of the vorticity vector (see Eq. 8) and the weighted average of the  $z$ -component of the  $\Lambda$ -polarization (see Eq. 7) at mid-rapidity.

Furthermore, we investigated the dependence of the  $z$ -component of the  $\Lambda$ -polarization ( $P^z$ ) with transverse momentum and the angular distance (in the transverse plane) from the partially quenched jet, which we present

in Fig. 4 as a color map. The markers indicate the positions of the  $|P^z|$ 's maxima in each  $p_T$ -bin. The  $|P^z|$ 's maxima are closer to the jet axis at high  $p_T$  than those at low  $p_T$  bins.

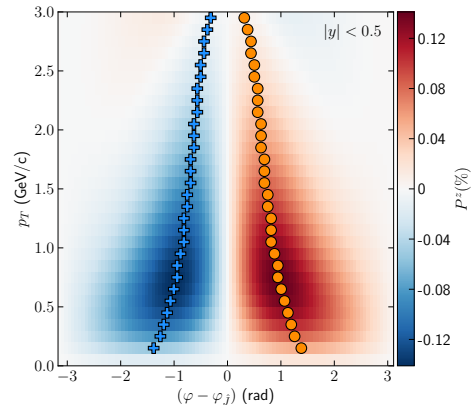


Figure 4: Distribution of the weighted average of the  $z$ -component of the polarization ( $P^z$ ), using  $\Lambda$ -multiplicity as weight and as function of  $p_T$  and the angular distance in the transverse plane. The average considers only data in the range  $|y| < 0.5$ . The orange/blue dots marks the bins where  $|P^z|$  is highest for that  $p_T$  bin.

### 3.2. The ring observable

We focused on the longitudinal component of polarization/vorticity for a jet that travels along the  $+\hat{x}$  direction. Since the transverse components are anti-symmetric with respect to rapidity/spatial-rapidity (see Fig. 2, right panel), they will average to zero in the above calculations and we lose information about them. However, the formation of a vortex ring due to our choice of initial condition has similarities with the vortex rings present in p+A collisions which were studied in Ref. [29]. There we introduced the ring observable  $\vec{\mathcal{R}}_\Lambda^{\hat{i}}$ , which we replicate below for completeness

$$\vec{\mathcal{R}}_\Lambda^{\hat{i}} \equiv \left\langle \frac{\vec{P}_\Lambda \cdot (\hat{i} \times \vec{p}_\Lambda)}{|\hat{i} \times \vec{p}_\Lambda|} \right\rangle_{p_T, y}. \quad (9)$$

Here,  $\hat{i} = \hat{J}$  is the axis direction of the jet<sup>2</sup>, and  $\langle \cdot \rangle_{p_T, y}$  denotes an weighted average over transverse momentum (in the range  $0.5 \text{ GeV}/c < p_T < 3.0 \text{ GeV}/c$ ) and rapidity (in the range  $|y| < 0.5$ ), using  $\Lambda$  multiplicity as

<sup>2</sup>on our calculation,  $\hat{J} = \hat{x}$

weight. The use of  $\overline{\mathcal{R}}_\Lambda^f$  will filter most contributions to the polarization which were not induced by the jet thermalization while allowing us to take into account effects in the direction besides  $\hat{z}$ . We will focus on  $\overline{\mathcal{R}}_\Lambda^f$  from now on.

The use of thermal vorticity, as shown in Eq. 7, has been debated in the literature [30, 31, 32]. There are three other definitions of vorticity which are popularly employed. The “kinetic vorticity” consists of the replacement  $\beta^\mu \rightarrow u^\mu$  and is appealing because it can be more intuitively interpreted. The “temperature vorticity” or “T-vorticity” relies on the replacement  $\beta^\mu \rightarrow Tu^\mu$  and also allows vorticity generation by temperature gradients. Finally, there is the “spatially projected kinetic vorticity” which replaces the derivative  $\partial^\mu$  by  $\nabla^\mu = (g^{\mu\nu} - u^\mu u^\nu)\partial_\nu$ . This has the effect of removing local acceleration terms from the kinetic vorticity. It also has a direct connection to the fluid vorticity in the non-relativistic limit. We show a comparison between the polarization results using these four different vorticity values in Fig. 5. The fact that polarization from kinetic, thermal, and temperature vorticities are essentially equal implies that in this case the vorticity is predominately generated by gradients in velocity, not in temperature. The higher value for the polarization from the spatially projected kinetic vorticity implies that local acceleration (caused mostly by the fluid expansion) has the effect of reducing the final  $\Lambda$  polarization.

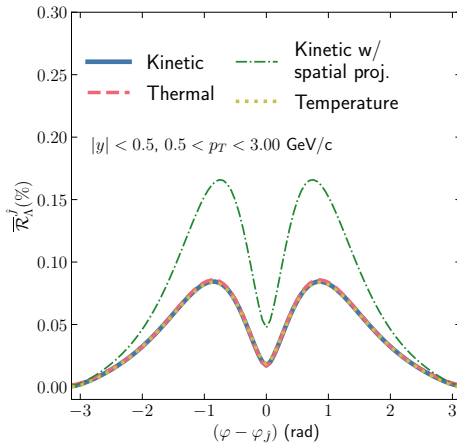


Figure 5:  $\overline{\mathcal{R}}_\Lambda^f$  (see Eq. 9) computed from  $\Lambda$ -polarization calculations using four types of vorticity tensor.

We study the sensitivity of the ring observable  $\overline{\mathcal{R}}_\Lambda^f$

on medium’s specific shear viscosity. In addition to  $\eta/s = 0.08$ , we perform calculations with  $\eta/s = 0.00, 0.01, 0.16$  and  $0.24$ . Figure 6 shows that the medium’s shear viscosity suppresses the ring observable  $\overline{\mathcal{R}}_\Lambda^f$ <sup>3</sup>. We observe a higher sensitivity of  $\overline{\mathcal{R}}_\Lambda^f$  to small viscosity values  $\eta/s < 0.08$  than  $\eta/s > 0.08$ . This trend is consistent with the vorticity ring being quenched by the medium, an effect which will be stronger for higher viscosity, but that eventually gets saturated. This is in contrast to elliptic flow, which has a more or less uniform dependence with viscosity [33].

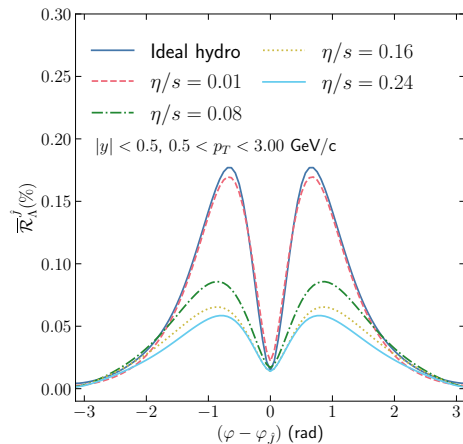


Figure 6: Distribution of  $\overline{\mathcal{R}}_\Lambda^f$  (see Eq. 9) for different specific shear viscosities.

It is possible to argue that a jet which is quenched at the center of the system will not be accompanied by an unquenched jet. Instead, there would be a pair of quenched jets, inducing a pair back-to-back vortex rings. One could approximately treat the medium excitation from the two quenched jets as independent superposition (after rotating one of them by  $\pi$  rad). However, this would neglect the possibility of interactions between the two vortices during the hydrodynamic evolution. We investigate the possibility of a double-quenched jet by displacing the energy-momentum deposition to  $x = 0.6$  fm. In the sequence, we add a second one at  $x = -0.6$  fm with momentum in the opposite direction of the first. We compare the superposition scenario with the full simulation in Fig. 7. It is clear

<sup>3</sup>The angle where the signal is strong has a small dependence on viscosity as well.

to see that the superposition scenario has a polarization which is almost double the one where we evolve the two quenched jets, indicating the interaction between them during hydrodynamic evolution is crucial and has a self-canceling effect.

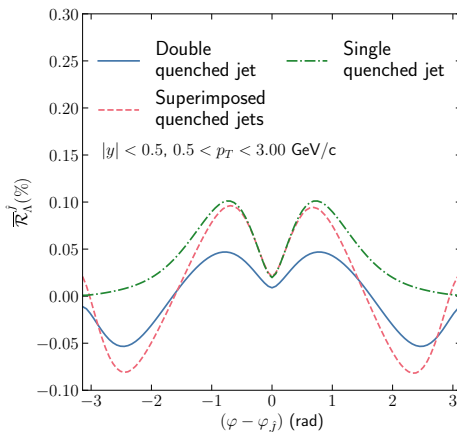


Figure 7: Comparison between the  $\bar{\mathcal{R}}_{\Lambda}^j$  in a double-quenched jet scenario versus the single-quenched jet case. The blue curve shows the result from the simulation and the red one by superimposing two single-quenched jets (shown in green).

#### 4. Conclusions

We modeled the thermalization of the energy-momentum from a hard parton as a “hot spot” which propagates inside fluid dynamic simulations. Such configuration of velocities will generate a vortex ring, which can be quantified by the vorticity of the fluid. The vorticity will lead to the emission of polarized hadrons on the particlezation hypersurface as described in [30, 15].

To obtain the energy and momentum deposited in the medium by the jet thermalization, we assumed a jet with a transverse momentum of 89.5 GeV/c that would deposit approximately 40% of its energy in the medium, motivated by [4, Fig. 3] and [22, Fig. 8]. The polarized hadron emission would accompany a partially quenched jet, meaning that experimentally any analysis aiming to measure this effect would have to focus on an asymmetric jet pair, with the higher momentum jet having momentum of the order of 90 GeV/c and the lower momentum being of order 60 GeV/c. Other options, such

as using high-momentum trigger particles, will also be investigated in future work.

We computed the polarization of the  $\Lambda$  hyperon due to the vorticity caused by our model of jet thermalization. We showed that, for this specific case, the effects are dominated by velocity gradients and thus there is little difference in using thermal vorticity versus other definitions which are often suggested in the literature. We also showed that the strength of the signal is highly sensitive to the fluid’s shear viscosity.

The angular distribution of the ring observable  $\bar{\mathcal{R}}_{\Lambda}^j$  in the transverse plane with respect to the quenched jet peaks in the range 0.5 rad to 1.0 rad, depending on transverse momentum. This position depends also on the shear viscosity as well, albeit in a more subtle way than the polarization amount. We also showed that the addition of a second quenched jet will not significantly affect the region where  $\bar{\mathcal{R}}_{\Lambda}^j$  peaks. Instead, it will only dampen the overall magnitude in addition of an expected additional lobe in the opposite direction.

We point out that, despite the effect being of the order of only a few tenths of a percentiles, the proposed ring observable  $\bar{\mathcal{R}}_{\Lambda}^j$  should be measurable by experiments, since it has the same magnitude as reported per ALICE and STAR for the global  $\Lambda$ -polarization [16, 34]. We also inspected the typical maximum value found for  $\bar{\mathcal{R}}_{\Lambda}^j$ . We found that  $\bar{\mathcal{R}}_{\Lambda}^j < 0.25\%$  always, peaking in the  $p_T$  range of 0.5 GeV/c <  $p_T$  < 1.0 GeV/c.

We devote a future study to quantify the effects of event-by-event fluctuations in the fluid on  $\bar{\mathcal{R}}_{\Lambda}^j$ .

We note that the discussed jet induced polarization effect requires both color opacity and rapid thermalization. Thus, it is very likely present in AA and might disappear in pp and pA collisions (which may have rapid thermalization, but very small opacity). Since the reference is a high momentum trigger rather than a global quantity like the reaction plane, it should be possible for experiments to examine events with one  $\Lambda$  and one high momentum triggered hadron to verify this effect. If it turns out that indeed  $\bar{\mathcal{R}}_{\Lambda}^j$  is non-zero for AA events, one could proceed to do more detailed model-data comparisons as a way to constrain viscosity and jet energy loss.

#### Acknowledgments

WMS, JGPB, DDC, JT and GT are supported by FAPESP projects 17/05685-2 (all), 19/05700-7 (WMS), 19/16293-3 (JPB) and 17/06508-7 (GT). MAL is supported by the U.S. Department of Energy grant DE-SC0020651 and acknowledges support of the Fulbright

Commission of Brazil. CS is supported by the U.S. Department of Energy under grant number DE-SC0013460 and the National Science Foundation under grant number PHY-2012922. GT acknowledges CNPQ bolsa de produtividade 301432/2017-1.

## References

- [1] M. Gyulassy, M. Plumer, Jet Quenching in Dense Matter, *Phys. Lett. B* 243 (1990) 432–438. doi:10.1016/0370-2693(90)91409-5.
- [2] X.-N. Wang, M. Gyulassy, Gluon shadowing and jet quenching in A + A collisions at  $s^{*}(1/2) = 200$ -GeV, *Phys. Rev. Lett.* 68 (1992) 1480–1483. doi:10.1103/PhysRevLett.68.1480.
- [3] U. A. Wiedemann, Jet Quenching in Heavy Ion Collisions, *Landolt-Bornstein* 23 (2010) 521. arXiv:0908.2306, doi:10.1007/978-3-642-01539-7\_17.
- [4] G. Aad, et al., Observation of a Centrality-Dependent Dijet Asymmetry in Lead-Lead Collisions at  $\sqrt{s_{NN}} = 2.77$  TeV with the ATLAS Detector at the LHC, *Phys. Rev. Lett.* 105 (2010) 252303. arXiv:1011.6182, doi:10.1103/PhysRevLett.105.252303.
- [5] S. Chatrchyan, et al., Observation and studies of jet quenching in PbPb collisions at nucleon-nucleon center-of-mass energy = 2.76 TeV, *Phys. Rev. C* 84 (2011) 024906. arXiv:1102.1957, doi:10.1103/PhysRevC.84.024906.
- [6] T. Schäfer, D. Teaney, Nearly Perfect Fluidity: From Cold Atomic Gases to Hot Quark Gluon Plasmas, *Rept. Prog. Phys.* 72 (2009) 126001. arXiv:0904.3107, doi:10.1088/0034-4885/72/12/126001.
- [7] K. Werner, I. Karpenko, M. Bleicher, T. Pierog, S. Porteboeuf-Houssais, Jets, Bulk Matter, and their Interaction in Heavy Ion Collisions at Several TeV, *Phys. Rev. C* 85 (2012) 064907. arXiv:1203.5704, doi:10.1103/PhysRevC.85.064907.
- [8] U. Heinz, R. Snellings, Collective flow and viscosity in relativistic heavy-ion collisions, *Ann. Rev. Nucl. Part. Sci.* 63 (2013) 123–151. arXiv:1301.2826, doi:10.1146/annurev-nucl-102212-170540.
- [9] C. Gale, S. Jeon, B. Schenke, Hydrodynamic Modeling of Heavy-Ion Collisions, *Int. J. Mod. Phys. A* 28 (2013) 1340011. arXiv:1301.5893, doi:10.1142/S0217751X13400113.
- [10] E. Shuryak, Strongly coupled quark-gluon plasma in heavy ion collisions, *Rev. Mod. Phys.* 89 (2017) 035001. arXiv:1412.8393, doi:10.1103/RevModPhys.89.035001.
- [11] C. Shen, L. Yan, Recent development of hydrodynamic modeling in heavy-ion collisions, *Nucl. Sci. Tech.* 31 (12) (2020) 122. arXiv:2010.12377, doi:10.1007/s41365-020-00829-z.
- [12] J.-P. Blaizot, Y. Mehtar-Tani, Jet Structure in Heavy Ion Collisions, *Int. J. Mod. Phys. E* 24 (11) (2015) 1530012. arXiv:1503.05958, doi:10.1142/S021830131530012X.
- [13] J. Takahashi, B. M. Tavares, W. L. Qian, R. Andrade, F. Grassi, Y. Hama, T. Kodama, N. Xu, Topology studies of hydrodynamics using two particle correlation analysis, *Phys. Rev. Lett.* 103 (2009) 242301. arXiv:0902.4870, doi:10.1103/PhysRevLett.103.242301.
- [14] B. Alver, G. Roland, Collision geometry fluctuations and triangular flow in heavy-ion collisions, *Phys. Rev. C* 81 (2010) 054905, [Erratum: *Phys.Rev.C* 82, 039903 (2010)]. arXiv:1003.0194, doi:10.1103/PhysRevC.82.039903.
- [15] F. Becattini, M. A. Lisa, Polarization and Vorticity in the Quark Gluon Plasma (3 2020). arXiv:2003.03640, doi:10.1146/annurev-nucl-021920-095245.
- [16] L. Adamczyk, et al., Global  $\Lambda$  hyperon polarization in nuclear collisions: evidence for the most vortical fluid, *Nature* 548 (2017) 62–65. arXiv:1701.06657, doi:10.1038/nature23004.
- [17] B. Betz, M. Gyulassy, G. Torrieri, Polarization probes of vorticity in heavy ion collisions, *Phys. Rev. C* 76 (2007) 044901. arXiv:0708.0035, doi:10.1103/PhysRevC.76.044901.
- [18] W. Ke, J. S. Moreland, J. E. Bernhard, S. A. Bass, Constraints on rapidity-dependent initial conditions from charged particle pseudorapidity densities and two-particle correlations, *Phys. Rev. C* 96 (4) (2017) 044912. arXiv:1610.08490, doi:10.1103/PhysRevC.96.044912.
- [19] J. E. Bernhard, Bayesian parameter estimation for relativistic heavy-ion collisions, Ph.D. thesis, Duke U. (4 2018). arXiv:1804.06469.
- [20] I. Karpenko, F. Becattini, Lambda polarization in heavy ion collisions: from RHIC BES to LHC energies, *Nucl. Phys. A* 982 (2019) 519–522. arXiv:1811.00322, doi:10.1016/j.nuclphysa.2018.10.067.
- [21] C. Young, B. Schenke, S. Jeon, C. Gale, Dijet asymmetry at the energies available at the CERN Large Hadron Collider, *Phys. Rev. C* 84 (2011) 024907. arXiv:1103.5769, doi:10.1103/PhysRevC.84.024907.
- [22] M. Aaboud, et al., Measurement of jet  $p_T$  correlations in Pb+Pb and pp collisions at  $\sqrt{s_{NN}} = 2.76$  TeV with the ATLAS detector, *Phys. Lett. B* 774 (2017) 379–402. arXiv:1706.09363, doi:10.1016/j.physletb.2017.09.078.
- [23] A. M. Sirunyan, et al., In-medium modification of dijets in PbPb collisions at  $\sqrt{s_{NN}} = 5.02$  TeV (1 2021). arXiv:2101.04720.
- [24] H. Li, L.-G. Pang, Q. Wang, X.-L. Xia, Global  $\Lambda$  polarization in heavy-ion collisions from a transport model, *Phys. Rev. C* 96 (5) (2017) 054908. arXiv:1704.01507, doi:10.1103/PhysRevC.96.054908.
- [25] B. Schenke, S. Jeon, C. Gale, (3+1)D hydrodynamic simulation of relativistic heavy-ion collisions, *Phys. Rev. C* 82 (2010) 014903. arXiv:1004.1408, doi:10.1103/PhysRevC.82.014903.
- [26] B. Schenke, S. Jeon, C. Gale, Higher flow harmonics from (3+1)D event-by-event viscous hydrodynamics, *Phys. Rev. C* 85 (2012) 024901. arXiv:1109.6289, doi:10.1103/PhysRevC.85.024901.
- [27] J.-F. Paquet, C. Shen, G. S. Denicol, M. Luzum, B. Schenke, S. Jeon, C. Gale, Production of photons in relativistic heavy-ion collisions, *Phys. Rev. C* 93 (4) (2016) 044906. arXiv:1509.06738, doi:10.1103/PhysRevC.93.044906.
- [28] A. Bazavov, et al., Equation of state in (2+1)-flavor QCD, *Phys. Rev. D* 90 (2014) 094503. arXiv:1407.6387, doi:10.1103/PhysRevD.90.094503.
- [29] M. A. Lisa, J. a. G. P. Barbon, D. D. Chinellato, W. M. Serenone, C. Shen, J. Takahashi, G. Torrieri, Vortex rings from high energy central p+A collisions (1 2021). arXiv:2101.10872.
- [30] F. Becattini, G. Inghirami, V. Rolando, A. Beraudo, L. Del Zanna, A. De Pace, M. Nardi, G. Pagliara, V. Chandra, A study of vorticity formation in high energy nuclear collisions, *Eur. Phys. J. C* 75 (9) (2015) 406, [Erratum: *Eur.Phys.J.C* 78, 354 (2018)]. arXiv:1501.04468, doi:10.1140/epjc/s10052-015-3624-1.
- [31] Y. B. Ivanov, A. Soldatov, Vortex rings in fragmentation regions in heavy-ion collisions at  $\sqrt{s_{NN}} = 39$  GeV, *Phys. Rev. C* 97 (4) (2018) 044915. arXiv:1803.01525, doi:10.1103/PhysRevC.97.044915.
- [32] I. Karpenko, Vorticity and Polarization in Heavy Ion Collisions: Hydrodynamic Models, 2021. arXiv:2101.04963.
- [33] P. Romatschke, U. Romatschke, Viscosity Information from Relativistic Nuclear Collisions: How Perfect is the Fluid Ob-

- served at RHIC?, Phys. Rev. Lett. 99 (2007) 172301. arXiv:0706.1522, doi:10.1103/PhysRevLett.99.172301.
- [34] S. Acharya, et al., Global polarization of  $\Lambda\bar{\Lambda}$  hyperons in Pb-Pb collisions at  $\sqrt{s_{NN}} = 2.76$  and 5.02 TeV, Phys. Rev. C 101 (4) (2020) 044611. arXiv:1909.01281, doi:10.1103/PhysRevC.101.044611.